

1 **A local-to-large scale view of Maritime Continent rainfall: control by ENSO,**  
2 **MJO and equatorial waves**

3 Simon C. Peatman\*, Juliane Schwendike, Cathryn E. Birch, John H. Marsham

4 *Institute for Climate and Atmospheric Science, School of Earth and Environment, University of*  
5 *Leeds, Leeds, UK*

6 Adrian J. Matthews

7 *Centre for Ocean and Atmospheric Sciences, School of Environmental Sciences and School of*  
8 *Mathematics, University of East Anglia, Norwich, UK*

9 Gui-Ying Yang

10 *National Centre for Atmospheric Science, Department of Meteorology, University of Reading,*  
11 *Reading, UK*

12 \*Corresponding author: Simon C. Peatman, Institute for Climate and Atmospheric Science, School  
13 of Earth and Environment, University of Leeds, Leeds, LS2 9JT, UK, earspe@leeds.ac.uk

## ABSTRACT

14 The canonical view of the Maritime Continent (MC) diurnal cycle is deep convection occurring  
15 over land during the afternoon and evening, tending to propagate offshore overnight. However,  
16 there is considerable day-to-day variability in the convection, and the mechanism of the offshore  
17 propagation is not well understood. We test the hypothesis that large-scale drivers such as ENSO,  
18 the MJO and equatorial waves, through their modification of the local circulation, can modify  
19 the direction or strength of the propagation, or prevent the deep convection from triggering in the  
20 first place. Taking a local-to-large scale approach we use *in situ* observations, satellite data and  
21 reanalyses for five MC coastal regions, and show that the occurrence of the diurnal convection  
22 and its offshore propagation is closely tied to coastal wind regimes we define using the ~~using the~~  
23 *k*-means cluster algorithm. Strong prevailing onshore winds are associated with a suppressed  
24 diurnal cycle of precipitation; while prevailing offshore winds are associated with an active diurnal  
25 cycle, offshore propagation of convection and a greater risk of extreme rainfall. ENSO, the MJO,  
26 equatorial Rossby waves and westward mixed Rossby-gravity waves have varying levels of control  
27 over which coastal wind regime occurs, and therefore on precipitation, depending on the MC  
28 coastline in question. The large-scale drivers associated with dry and wet regimes are summarised  
29 for each location as a reference for forecasters.

30 *Significance statement.* Extreme precipitation can be life-threatening in the Maritime Continent  
31 region, for example due to flash floods and landslides. The main form of variability of convective  
32 storms is the diurnal cycle, but this can be modulated by large-scale weather drivers. By quantifying  
33 the effect of these drivers on local-scale weather regimes for a range of Maritime Continent  
34 locations, we identify which drivers are most important (and in which phase) to consider when  
35 understanding the local risk of extreme rainfall. Given that these large-scale drivers may be forecast  
36 with greater skill than is possible for quantitative precipitation forecasts, this study provides crucial  
37 extra information for forecasters to aid prediction of life-threatening weather conditions.

## 38 **1. Introduction**

39 The Maritime Continent (MC; figure 1), the archipelago situated on the equator between 90°E  
40 and 160°E, experiences some of the most intense rainfall on Earth, due to its location in the  
41 Indo-Pacific warm pool (Ramage 1968). Convection exhibits a strong diurnal cycle driven by the  
42 land-sea temperature contrast, with the heaviest rainfall over land generally occurring in the late  
43 afternoon and evening, and over ocean in the early morning. In some regions, such as south-west of  
44 Sumatra, north-west of Borneo, north and south of Java, and north of New Guinea, convection can  
45 propagate offshore overnight (e.g., Qian 2008; Love et al. 2011). Several physical mechanisms have  
46 been proposed for the nocturnal offshore propagation, including roles for gravity waves (Warner  
47 et al. 2003; Mapes et al. 2003; Love et al. 2011; Hassim et al. 2016), cold pool outflow (Mori et al.  
48 2004; Wu et al. 2009) and the land-sea breeze circulation (Houze et al. 1981).

49 The diurnal convection and its propagation vary in strength day-to-day, and on some days at any  
50 given location in the MC it may not occur at all. We use a novel local-to-large scale framework, as  
51 explained below, to investigate the hypothesis that these forms of local variability are influenced

52 by large-scale drivers through their control on the local circulation, and to quantify the relative  
53 contributions of such drivers for a range of locations in the MC.

54 Previous work has shown an interaction between the diurnal cycle and the intraseasonal  
55 Madden-Julian Oscillation (MJO; e.g., Oh et al. 2012; Peatman et al. 2014; Birch et al. 2016;  
56 Vincent and Lane 2016; Sakaeda et al. 2020; Qian 2020; Muhammad et al. 2021). The MJO  
57 consists of alternating large-scale envelopes of active and suppressed convection, propagating  
58 slowly eastwards at the equator, from the Indian Ocean across the MC into the Pacific (Madden and  
59 Julian 1971, 1972). Changes in the diurnal cycle account for 81% of the variability in land-based  
60 precipitation during an MJO cycle, with the largest diurnal amplitude occurring just ahead of the  
61 active MJO envelope (Oh et al. 2012; Peatman et al. 2014).

62 The El Niño-Southern Oscillation (ENSO) also modulates the MC diurnal cycle, enhancing it  
63 during El Niño events and suppressing it during La Niña events. As a result, even though El Niño  
64 suppresses MC convection and La Niña enhances MC convection on the large scale, precipitation  
65 anomalies over the islands have the opposite sign (Rauniyar and Walsh 2013). Several types of  
66 convectively-coupled equatorial wave also modulate the diurnal cycle as they propagate through  
67 the MC, affecting the probability of extreme rainfall (Ferrett et al. 2020; Lubis and Respati 2021).  
68 According to Sakaeda et al. (2020), equatorial Kelvin waves predominantly modulate the diurnal  
69 amplitude over ocean and over land to a lesser extent, with the strongest convection leading the  
70 active convection phase of the wave. Baranowski et al. (2016) showed that Kelvin waves may  
71 enhance the diurnal cycle over Sumatra and Borneo depending on the time of day of their arrival,  
72 due to phase locking. Sakaeda et al. (2020) also showed equatorial Rossby waves modulate the  
73 diurnal cycle more strongly over ocean than land; and over land the strongest diurnal cycle leads  
74 the convective phase of the wave on the east side of islands, but lags on the west side. Nocturnal  
75 offshore propagation of convection from south-west Sumatra, north-west Borneo and south Java

76 is enhanced by the active phase of a Kelvin wave; Ahead of the convective phase of a Rossby  
77 wave, while the propagation is enhanced for south-west Sumatra and suppressed for north-west  
78 Borneo ~~ahead of a Rossby wave~~.

79 In diagnosing such scale interactions, most studies use a large-to-local scale approach,  
80 compositing local conditions as a function of the large-scale state. However, the diurnal cycle  
81 is still variable even within an MJO phase. An example is the offshore propagation south-west  
82 of Sumatra, which is strongest in a composite sense during MJO phase 2, but on any individual  
83 day during that phase the propagation may be weak or non-existent. This means the large-to-local  
84 scale approach is of limited use for forecasters. Given the potential for convection in this region to  
85 produce dangerous and possibly life-threatening conditions (e.g., Xavier et al. 2014; Ferrett et al.  
86 2020; Mohd Nor et al. 2020; Lubis and Respati 2021), we require further metrics.

87 Therefore, we adopt a local-to-large scale approach, considering first the local conditions  
88 associated with propagating convection, before understanding how these local regimes are set  
89 up by phenomena at larger scales. This novel approach, combined with the use of *in situ* data from  
90 one of the few intensive atmospheric field campaigns to have been carried out in the region, allows  
91 us to quantify the large-scale drivers' influence on the coastal winds over several MC locations; and  
92 thus document which large-scale drivers are key to determining when and where intense convection  
93 associated with extreme rainfall is likely to occur.

## 94 **2. Data and methods**

### 95 *a. Field campaign observations*

96 We use observations from two Japanese field campaigns associated with the Years of the Maritime  
97 Continent (YMC; Yoneyama and Zhang 2020) International programme, located around Bengkulu

98 in Sumatra (figure 1). These are referred to as “pre-YMC” (2015 campaign, November–December  
99 2015) and “YMC” (2017 campaign, November 2017 – January 2018). We use radiosonde  
100 observations of wind from both campaigns from Bengkulu, from 2015/11/09 to 2015/12/25 and  
101 2017/11/16 to 2018/01/15 (108 days in total). Radiosondes were released every 3 hours at 00, 03,  
102 . . . , 21 UTC; or 07, 10, 13, 16, 19, 22, 01, 04 local time (LT), taking LT to be UTC+7. Data are  
103 linearly interpolated to the same pressure levels as used in the European Centre for Medium-range  
104 Weather Forecasting (ECMWF) Fifth Reanalysis (ERA5; Hersbach et al. 2020; see below).

#### 105 *b. Other data sets*

106 To diagnose precipitation, including the offshore propagation of rainfall, Global Precipitation  
107 Measurement (GPM; Heale et al. 2019) data sets are used. GPM data are provided every 30 minutes  
108 on a  $0.1^\circ \times 0.1^\circ$  grid. The “high-quality” data set (GPM-HQ) uses intercalibrated observations  
109 from passive microwave (PMW) instruments on a number of satellites, which are gridded then  
110 further calibrated using monthly gauge accumulations. The PMW satellites are largely “satellites  
111 of opportunity” (that is, their orbits, operations and so on are out of the control of the GPM mission)  
112 and there are missing regions between swaths. The Integrated Multi-satellitE Retrievals for GPM  
113 (IMERG) algorithm fills these gaps to provide a complete gridded product, at the same temporal  
114 and spatial resolutions. We use IMERG version 06, which fills gaps by morphing the GPM-HQ  
115 data according to motion vectors derived from total column water vapour in the Modern-Era  
116 Retrospective analysis for Research and Applications, version 2 (MERRA-2; Gelaro et al. 2017).

117 Where possible, we use GPM-HQ as this includes only the direct measurements of precipitation  
118 from PMW instruments (with calibration). When producing composites over a long time period  
119 ( $O(10^2)$  or more days), the effects of missing data are negligible. However, when the number of  
120 days is small ( $O(10^1)$ ) we use IMERG, to benefit from the improved data coverage. We use GPM

121 during December, January and February (DJF) for the period of its availability, from DJF 2000/01  
122 to 2019/20. For simplicity, we always exclude 29 February from DJF.

123 When extending our analysis beyond the field campaign periods, where possible we use hourly  
124 ERA5 for all 41 available DJFs, from 1979/80 to 2019/20. ERA5 is on a 0.25° grid. We also use the  
125 ECMWF interim reanalysis (ERA-Interim; Dee et al. 2011) when comparing wind values against  
126 those in equatorial waves (see below). MJO phases are defined using the Realtime Multivariate  
127 MJO (RMM) indices (Wheeler and Hendon 2004). To investigate the effect of ENSO we use  
128 the Oceanic Niño Index (ONI; Climate Prediction Center 2020) version 5, which is the 3-month  
129 running mean of the monthly Niño3.4 anomaly (with the subtracted climatology being a 30-year  
130 mean updated every 5 years). El Niño and La Niña events are defined as a period of at least  
131 5 months with  $\text{ONI} \geq 0.5^\circ\text{C}$  or  $\leq -0.5^\circ\text{C}$ , respectively. All other times are defined as neutral  
132 ENSO phase. We also analyse tropical cyclone (TC) tracks, using the International Best Track  
133 Archive for Climate Stewardship (IBTrACS; Knapp et al. 2010).

134 We use a data set of equatorial waves identified using the methodology of Yang et al. (2003) and  
135 described in Ferrett et al. (2020). Wind and geopotential height data are regridded to a 1° grid and  
136 filtered to retain variability with period 2–30 days and zonal wavenumbers 2–40. Eastward- and  
137 westward-components are separated out in wavenumber-frequency space and projected onto the  
138 theoretical horizontal structures of equatorial Kelvin,  $n = 1$  Rossby (R1),  $n = 2$  Rossby (R2) and  
139 westward mixed Rossby-gravity (WMRG) waves, using a meridional trapping scale of  $6^\circ$  (Yang  
140 et al. 2003). This is performed using ERA-Interim from 1997 to 2018, separately at each pressure  
141 level. The resulting data set consists of the wind and geopotential height anomaly contributions  
142 from each wave type.

143 *c. k-means clustering*

144 To differentiate between coastal wind regimes, the  $k$ -means clustering algorithm is used  
145 (MacQueen 1967).  $k$ -means is an iterative algorithm which sorts data points into clusters by  
146 minimizing the total Euclidean distance between a cluster's data points and their mean. For example,  
147 in section 3a we cluster zonal wind  $u$  from 108 days of 3-hourly radiosondes, concatenating the  
148 8 sondes each day to produce a field of shape 108 days  $\times$  8 times of day  $\times$  16 pressure levels.  
149 We use  $k$ -means to sort each day into a cluster, hence we are clustering 108 data points in  
150  $8 \times 16 = 128$ -dimensional space.

151 The number of clusters  $k$  is an *a priori* choice which is made subjectively, albeit with physical  
152 justifications as detailed in the text, having run the algorithm for a range of  $k$  values. The  
153 initialization of the algorithm is random, with no guarantee that different initializations will  
154 converge to the same result. Therefore, a number of initializations are performed and the best  
155 solution is selected (i.e., that which produces the minimal total Euclidean distance). For field  
156 campaign data, 500 initializations are performed; when extending to 41 DJFs, this is increased to  
157 20,000. These values were chosen by experiment as sufficient to make the results of the clustering  
158 robust. To avoid confusion, we label the clusters from observations (section 3a) as 0, 1,  $\dots$ ,  
159  $(k - 1)$ ; and the clusters from reanalysis (sections 3b,c) as A, B,  $\dots$ . Coastal wind clusters are  
160 always ordered by the mean value of the cluster centre field, from the most strongly onshore to the  
161 most strongly offshore.

162 *d. Coastal wind associated with large-scale drivers*

163 To investigate possible large-scale causes of the coastal wind regimes derived from  $k$ -means  
164 clustering, we quantify the contribution of several large-scale drivers to the wind at a given coastal  
165 location using the following methods. ERA-Interim is used throughout for consistency since it is



166 the reanalysis used in the equatorial waves data set. Here we assume the required coastal wind is  
 167  $u_{850}$ , although the same technique is also applied to meridional wind  $v_{850}$  for certain coastlines.  
 168 The 850 hPa level is chosen as it is one of the levels used in the RMM indices to monitor the MJO  
 169 and it is representative of all levels of the wind clusters.

170 For Kelvin, R1, R2 and WMRG waves we take  $u'_{850}$ , where the prime denotes an anomaly,  
 171 directly from the equatorial waves data set (see section 2b) and average along the nominal coastline  
 172 in the respective coloured box in figure 1.

173 To derive a  $u'_{850}$  value associated with ENSO, we take the monthly ONI values and, to avoid  
 174 having a sharp jump at the start of each month, apply a 31-day running mean. We take the daily  
 175 mean ERA-Interim  $u_{850}$  averaged along the nominal coastline and subtract the climatology and  
 176 leading 3 harmonics of the seasonal cycle to produce a time series of  $u'_{850}$ . We take these  $u'_{850}$   
 177 values and the daily smoothed ONI values, for all 39 available DJFs (1979/80 to 2017/18), and  
 178 perform least-squares linear regression:

$$u'_{850}(t) = m_{\text{ONI}} \times \text{ONI}(t) + c_{\text{ONI}}, \quad (1)$$

179 where  $t$  is time, and  $m_{\text{ONI}}$  and  $c_{\text{ONI}}$  are the parameters to be fitted.

180 Similarly, we perform linear regression with the RMM indices to find  $u'_{850}$  associated with the  
 181 MJO. However, because there are two RMMs we need to perform multiple linear regression and  
 182 because they are not independent we need to include a cross-term, which represents the fact that  
 183 the prevailing wind at the coast does not necessarily blow in opposite directions in opposite MJO  
 184 phases:

$$u'_{850}(t) = m_1 \times \text{RMM1}(t) + m_2 \times \text{RMM2}(t) + m_3 \times \text{RMM1}(t) \times \text{RMM2}(t) + c_{\text{RMM}}, \quad (2)$$

185 where  $m_1$ ,  $m_2$ ,  $m_3$  and  $c_{\text{RMM}}$  are the parameters to be fitted, and the RMM time series are taken  
 186 from Wheeler and Hendon (2004). Note that, although  $u'_{850}$  is not modelled as a linear function of

187 the RMMs, equation 2 is linear in the fitted parameters, so least-squares multiple linear regression  
188 can be used to find the parameter values.

### 189 **3. Results**

#### 190 *a. Pre-YMC and YMC field campaign observation periods*

191 This section of the analysis uses observations from the field campaigns on the south-west coast  
192 of Sumatra. Several of the possible mechanisms for offshore propagation of convection mentioned  
193 in section 1 depend either directly or indirectly on land-sea breezes. Therefore, we explore the  
194 variability in land-sea breeze and its relation to diurnal convection, including offshore propagation.  
195 We also wish to investigate the development of each land-sea breeze regime in terms of large-scale  
196 phenomena. Since phenomena such as the MJO and most equatorial waves are (close to the  
197 equator) predominantly associated with variations in zonal not meridional wind, we analyse the  
198 zonal component  $u$  only at this stage. The zonal and meridional components were also rotated to  
199 onshore and alongshore components, and the the analysis repeated using the onshore component  
200 only (not shown); this did not substantially change the results.

201 We take  $u$  from the 108 days of 3-hourly radiosondes at Bengkulu, performing  $k$ -means clustering  
202 as described in section 2c. By experiment, it was found that  $k = 3$  best represents the land-sea  
203 breeze regimes (figures 2a–c; other  $k$  values not shown). This achieves the best balance between  
204 separating out physically distinct regimes (with  $k = 2$  being too few) while preserving a reasonable  
205 sample size for each cluster (for  $k = 4$ , one of the clusters has only 4 days). Moreover, with  $k = 4$   
206 two of the clusters are very similar to cluster 0 in figure 2a so are not physically distinct.

207 The clusters consist of strong onshore winds all day (cluster 0), moderate onshore winds all day  
208 (cluster 1) and offshore winds all day except near to the ground in the afternoon (cluster 2). The

209 diurnal anomaly profiles of  $u$  (relative to the cluster's own daily mean profile; figures 2d–f) are  
210 broadly similar for each cluster, but the daily mean is sufficiently different that only the offshore  
211 cluster (2) has an absolute change in wind direction at any level (figure 2c). The diurnal anomalies  
212 show all three clusters have the strongest onshore wind in the afternoon, but slightly earlier (13 LT)  
213 in the offshore cluster (2) than in the onshore clusters (0 and 1; 16 LT). The strong land-sea breeze  
214 is shallow, reaching up to around 925 hPa, close to a typical boundary layer depth over ocean.  
215 However, in the onshore clusters (0 and 1) the wind is onshore at all levels shown at the time of the  
216 strongest sea breeze, whereas the offshore cluster (2) has a return flow between 925 and 775 hPa at  
217 this time.

218 The clustering of the land-sea breeze is a valuable tool as it neatly divides the days into distinct  
219 diurnal convection regimes. Figure 3 shows the composite diurnal cycle of precipitation as  
220 Hovmöller diagrams using IMERG data in the red dashed box of figure 1, averaged along the  
221 coastline direction. The diagrams are composited over each cluster, with time of day running  
222 down the page and extended 12 hours into the next day, to capture the full offshore propagation.  
223 Distances on the horizontal axis are negative offshore (to the south-west) and positive onshore (to  
224 the north-east).

225 Although all three clusters have a discernible diurnal cycle over both land and sea, the offshore  
226 cluster (2) alone exhibits the canonical view of heavy precipitation (around  $2 \text{ mm hr}^{-1}$ ) over land  
227 near the coast at 13–19 LT, propagating offshore during the evening and night-time. All the  
228 precipitation over the sea is associated with this propagation, which extends into the following  
229 afternoon. There appear to be two modes of propagation, causing the propagation region to widen  
230 from about 19 LT onwards, with the two modes becoming distinct around 04–07 LT. Preceding the  
231 convection is a corresponding propagating region of suppressed conditions.

232 In the strong onshore cluster (0) the propagation is mostly in the same direction as the wind,  
233 progressing inland before continuing to propagate over the sea to the north-east of Sumatra.  
234 Precipitation over the sea reduces in the afternoon and evening but is on a larger scale than the  
235 organised propagation in the offshore cluster (2), suggesting it is associated with a large-scale  
236 phenomenon such as the MJO. Precipitation over land does not feature a strong burst near the coast  
237 in the afternoon and evening as in the offshore cluster (2), indicating a suppression of the canonical  
238 diurnal cycle. Cluster 1 has features which are elements of each of the other clusters, with coherent  
239 propagation inland and weak precipitation propagating offshore. While the offshore cluster (2) has  
240 strong convection on the sea-facing flanks of the mountains (see orography at the bottom of the  
241 plot), the strongest precipitation in the moderate onshore cluster (1) is inland, the other side of the  
242 mountain range. Hence, the stronger convection always favours the leeward side of the mountains.

243 To investigate possible large-scale causes of the coastal wind regimes and therefore understand  
244 which large-scale conditions can lead to each convection regime, we consider the zonal wind at  
245 Bengkulu associated with a number of large-scale drivers and compare them to the total wind.  
246 Daily mean  $u'_{850}$  values associated with several drivers are computed as described in section 2d  
247 and shown in figure 4. The linear regression of  $u'_{850}$  onto ONI (equation 1) to derive the ENSO  
248 contribution is shown in figure 5a. The plot shows considerable variability in  $u'_{850}$  which is not  
249 explained by variability in ONI, due to other factors (which, according to our hypothesis, are  
250 mainly the other large-scale drivers in figure 4). By modelling the response to ENSO as linear  
251 and regressing onto ONI, we aim to estimate the contribution to  $u'_{850}$  which arises from ENSO  
252 forcing alone. Similarly, multiple linear regression of  $u'_{850}$  onto the RMM indices was performed  
253 (equation 2) to find the MJO contribution and the resultant surface in RMM space is shown as a  
254 contour plot in figure 5b.

255 Time series are plotted for ENSO (dark green curve), the MJO (dark blue), Kelvin (orange),  
256 R1 (dark pink), R2 (light pink) and WMRG (light blue). If the large-scale drivers described here  
257 account for the total wind field, then the sum of the six coloured curves and the mean seasonal cycle  
258 (climatology plus leading 3 harmonics; ~~thin black dotted~~ curve in figure 4), which is shown by  
259 the ~~thick black solid~~ curve, should match the total field shown in grey. During the 2015 campaign  
260 (figure 4a) there is a close match between the two. For approximately the first month of the  
261 campaign the wind was offshore and all days were in the cluster 2 except 26 and 27 November,  
262 when the wind was moderately onshore in cluster 1. The time series show this was caused by an  
263 R1 wave propagating through the region. From 12 December onwards the winds again shifted  
264 to being onshore, with all days being in cluster 1 or 0. On these days the sum of the large-scale  
265 contributions ~~in~~(~~thick black~~) does not match the total field so well, but both are positive and the  
266 strongest contribution is from the MJO. As discussed in section 2d, the MJO  $u'_{850}$  may be less  
267 accurate than for the other drivers considered, which may explain the discrepancy between the  
268 ~~thick black~~ and grey curves on these days. However, the MJO  $u'_{850}$  calculation is still sufficiently  
269 accurate to indicate days when the MJO is chiefly responsible for the coastal wind regime, such as  
270 the example discussed here.

271 In the 2017 campaign (figure 4b) there were no offshore cluster (2) days. The main difference  
272 between the two campaigns was an El Niño event in 2015/16 and a La Niña event in 2017/18.  
273 Hence, the  $u'_{850}$  contribution from ENSO is approximately  $-3.5 \text{ m s}^{-1}$  in the 2015 campaign and  
274 approximately  $+1.3 \text{ m s}^{-1}$  in the 2017 campaign. Individual peaks and troughs in the grey and  
275 ~~solid~~~~thick~~ black curves for the 2017 campaign tend to match each other, with the Kelvin, R1  
276 and R2 waves generally dominating variability on time scales of under a week. There are some  
277 periods when the magnitude of the grey and ~~solid~~~~thick~~ black curves differ considerably, such as  
278 22–30 November and 4–15 January. Such periods tend to have either a strong MJO signal or a

279 nearby TC (any day with a TC centre within  $10^\circ$  geodesic of Bengkulu according to IBTrACS is  
280 shown with a red star).

281 Thus, we have examples from the field campaign periods of ENSO, the MJO and equatorial  
282 waves (although there is no considerable contribution from WMRG waves) controlling the coastal  
283 wind regimes at Bengkulu (figure 4); and we find that these coastal wind regimes themselves  
284 determine the regimes of the diurnal cycle of convection (figure 3). In the following subsection we  
285 extend the analysis beyond the field campaign periods and perform a more quantitative analysis of  
286 the contributions of the large-scale drivers.

#### 287 *b. Extension to 41 DJFs along Sumatran coastline*

288 Although the analysis thus far has the advantage of using *in situ* observations to determine the  
289 wind regimes, it is limited to a few weeks in just two boreal winters, and is based on wind at a  
290 point location. Using ERA5 we now extend the analysis spatially and temporally. To confirm  
291 that ERA5 is an appropriate research tool for this study, we take ERA5  $u$  at Bengkulu on the  
292 108 field campaign days and perform  $k$ -means clustering again (not shown), to compare against the  
293 radiosonde clusters in figure 2. The results are very similar, although the ERA5 land-sea breeze  
294 circulation is slightly weaker and deeper than in the radiosondes. Therefore, we accept that the  
295 land-sea breeze in ERA5 is verified by the observations and we are confident that ERA5 is realistic  
296 enough to use it for our analysis.

297 We restrict ourselves to DJF, matching approximately the season already considered in section 3a,  
298 but extend the analysis to the 41 DJFs available in ERA5, going back to December 1979.  
299 Furthermore, noting that convection tends to be spatially heterogeneous and wanting to capture as  
300 much of the convection and its propagation as possible, we extend the analysis region to the entire

301 solid red box in figure 1. Thus we cover as much of the coastline as possible where it is fairly  
302 straight whilst avoiding Siberut, the largest of the Mentawai Islands just offshore from Sumatra.

303 We take hourly ERA5  $u$  averaged along the nominal west coastline of Sumatra indicated by the  
304 thick red line in figure 1 and cluster the 3,690 days from DJFs 1979/80 to 2019/20 (excluding  
305 29 February for simplicity). Whereas for point data at Bengkulu we chose  $k = 3$  to give us distinct  
306 physical regimes, for this case it was found by experiment that  $k = 4$  was preferable (figures 6a–d),  
307 and we label these A, B, C and D. Clusters A (strong onshore) and D (offshore) correspond to  
308 clusters 0 and 2 respectively in figures 2a,c but are spatially smoother due to averaging over more  
309 days. Clusters B (moderate onshore) and C (weak onshore) both roughly correspond to cluster 1 in  
310 figure 2b. These two clusters, and in particular their corresponding offshore Hovmöller diagrams  
311 of precipitation (figures 7b,c – see below), are distinct enough to warrant both being included in the  
312 analysis without either suffering from a small sample size (indeed, they are the two most frequent  
313 clusters).

314 The diurnal anomalies for each cluster (figures 6e–h) are very similar to each other, with daytime  
315 onshore winds beginning at low levels and rapidly spreading to higher levels in all cases. This is  
316 unlike the observed diurnal anomalies in figures 2d–f. In observations, the differences in diurnal  
317 anomalies between clusters may be due to errors associated with the convective parametrization  
318 scheme in the ERA5 model (e.g., Birch et al. 2015; Love et al. 2011); land-air feedbacks which the  
319 ERA5 model is unable to capture; or the small sample size if these anomalies vary considerably  
320 between days.

321 To create the Hovmöller diagrams of precipitation (figure 7) we use GPM-HQ, since we are  
322 compositing over enough days for the lesser data coverage to be unimportant. Both the strong and  
323 moderate onshore clusters (A and B) exhibit large-scale precipitation over the sea with almost all  
324 propagation being inland. The weak onshore cluster (C), although similar to cluster B in the  $u$

325 field, is not associated with large-scale heavy rain over the sea. The weak onshore (C) and offshore  
326 (D) clusters, while very different in  $u$ , have similar precipitation Hovmöller diagrams, differing  
327 only in that inland propagation is stronger than offshore for cluster C, and *vice versa* for cluster D.

328 The probability of extreme precipitation, defined here as exceeding the 99<sup>th</sup> percentile for the  
329 daily mean DJF, varies by cluster (figure 8). In the weak onshore (C) and offshore (D) clusters, over  
330 the south-west coast and just offshore, the probability of extreme rainfall can be around 50% more  
331 than average (over 70% more in some areas). In the strong and moderate clusters (A and B) the  
332 probability is reduced by a similar amount. Where there is a greater chance of extreme rainfall over  
333 and around the south-west coast region in clusters C and D, the Hovmöller diagrams in figure 7  
334 show that these are due to precipitation systems forming over land and propagating offshore, not  
335 propagating in from the sea.

336 The results of section 3a suggest ENSO and the MJO each play a role in determining the coastal  
337 wind regime at Bengkulu. Now, with a much larger data set, we examine the relationship between  
338 these phenomena and the wind clusters for the full south-west Sumatra coast. Figure 9a shows  
339 the number of days in each ENSO phase and figure 9b shows the same separated out by cluster.  
340 Consistent with the findings from the field campaigns (figure 4), La Niña events are more often  
341 associated with more onshore wind (accounting for 52% of the strong onshore cluster (A) days)  
342 and El Niño events with more offshore wind (58% of the offshore cluster (D) days). The large-scale  
343 circulation component of ENSO consists of a strengthened Walker circulation during La Niña and  
344 weakened during El Niño, so La Niña events are associated with large-scale ascent over the MC  
345 and El Niño with large-scale suppression. Therefore, we expect large-scale convergence into the  
346 MC region in the lower troposphere during La Niña events, consistent with winds blowing onshore  
347 over the south-west coast of Sumatra; and large-scale divergence out of the MC during El Niño,  
348 consistent with winds blowing offshore.



349 Figures 9c,d show the equivalent statistics for the MJO. Days with RMM amplitude  $< 1$  are shown  
350 in grey as “no MJO”. See the figure caption for a list of regions experiencing active large-scale  
351 convection in each MJO phase. Cluster A, with the strongest onshore wind and weakest diurnal  
352 cycle of precipitation, favours phases 4–6 (each accounting for 15–25% of cluster A days); while  
353 cluster D, with offshore wind and the strongest diurnal cycle of precipitation, favours phases 8  
354 and 1–3 (11–15% of cluster D days). This is consistent with existing theories of MJO propagation,  
355 with surface easterlies which blow offshore from Sumatra occurring ahead of the MJO when it  
356 is over the Indian Ocean (e.g., Matthews 2000). It is also consistent with Peatman et al. (2014),  
357 who showed the strongest diurnal cycle occurs just to the east of the active MJO; and the diurnal  
358 cycle is most greatly suppressed just ahead of the suppressed MJO. Here we see the offshore wind  
359 regime, associated with a strong diurnal cycle, favouring MJO phases when the active envelope  
360 is propagating through the Indian Ocean and approaching the MC, with this regime becoming far  
361 less common once the envelope reaches the MC in phases 4 and 5. Similarly the onshore wind  
362 regime, with a suppressed diurnal cycle, favours MJO phases when the active envelope has already  
363 propagated through the western MC where Sumatra is located, and is propagating into the west  
364 Pacific Ocean, with the suppressed envelope now approaching Sumatra.

365 Although figure 9 shows some correspondence between the clusters and both ENSO and the MJO,  
366 there are examples of every ENSO phase and every MJO phase coinciding with every wind cluster  
367 (although some are so rare that they are difficult to discern in the plot). Hence, while previous  
368 studies such as Rauniyar and Walsh (2013), Rauniyar and Walsh (2011) and Peatman et al. (2014)  
369 demonstrate the variation of the diurnal cycle by large-scale environment in a composite sense,  
370 we show here that ENSO or MJO phase do not uniquely determine the diurnal cycle regime and,  
371 from an operational forecasting perspective, is not sufficient information to issue a forecast of the  
372 likelihood or otherwise of severe thunderstorms in our region of interest. This very concern is

373 why in section 1 we chose a local-to-large scale approach by examining the local diurnal cycle and  
374 understanding what large-scale conditions are associated with different regimes, as opposed to the  
375 large-to-local scale approach of other studies.

376 Section 3a also showed equatorial waves partially determine the wind cluster. Figures 10b,g  
377 show composites of wind and geopotential height anomalies at 850 hPa summed over all four of  
378 the identified equatorial wave types (clusters A and D only) for the period covered by the waves data  
379 set (1997/98 to 2017/18), which is a subset of the ERA5 period. For comparison, the composite  
380 wind anomaly from ERA-Interim (the same reanalysis as was used for the wave identification) is  
381 shown in figures 10a,f. If the wind field in these clusters were determined entirely by the identified  
382 equatorial waves then panels (a) and (b) would match, as would panels (f) and (g). In fact, we  
383 have already seen that ENSO and the MJO also contribute to determining the wind regime, but  
384 there are broad similarities between the ERA-Interim composites and the wave composites which  
385 confirm the waves also have a substantial contribution. Note that the ERA-Interim composites  
386 have a considerably larger amplitude than the wave composites due to the filtering applied before  
387 the identification of the waves, as explained in section 2b. Applying the same filtering before  
388 compositing the winds as in figures 10a,f (not shown) gives values of similar amplitude to the wave  
389 composites, as well as removing some features not associated with the waves.

390 In the strong onshore cluster (A; figure 10b) there are cyclonic circulation patterns either side  
391 of the equator, slightly stronger and with a larger zonal extent in the southern hemisphere, which  
392 are also seen in figure 10a. In the offshore cluster (D; figure 10g) there is an anti-cyclone in  
393 the southern hemisphere and a small region of anti-cyclonic vorticity around 5°N, 90°E in the  
394 northern hemisphere. Again, the southern hemisphere vorticity in figure 10f is in approximately  
395 the same location, and the vorticity in the northern hemisphere is weak but also visible, albeit  
396 slightly further north (around 10°N). The asymmetry about the equator, with stronger anomalies in

397 the southern hemisphere, is because the clustering is performed over the southern half of Sumatra  
398 only. Southern hemisphere structures are more coherent in the composites whereas any variability  
399 between hemispheres causes northern hemisphere structures to be partially averaged over.

400 Figures 10c,h, 10d,i and 10e,j show, respectively, the Kelvin, R1 and R2 contributions to  
401 figures 10b,g. The WMRG contribution (not shown) is negligible. Figures 10d,i indicate the  
402 onshore wind regime is associated with the low-pressure (cyclonic) phase of an R1 wave and the  
403 offshore regime with the high-pressure (anti-cyclonic) phase. R1 is the largest contributor to the  
404 total wave composites in figures 10b,f. The theoretical R1 structure is symmetrical about the  
405 equator in geopotential height, while R2 is anti-symmetric. Therefore, if the real circulation has  
406 some asymmetry it can project onto both R1 and R2. Here, R2 reinforces the R1 signal in the  
407 southern hemisphere, where the analysis region is located (see figure 1) and opposes it in the  
408 opposite hemisphere, due to R1 being more coherent in the hemisphere of the analysis region.  
409 Given how precisely the pressure centres of R1 and R2 line up in longitude, we conclude that the  
410 projection onto both R1 and R2 arises from the same circulation pattern, which mostly resembles  
411 the theoretical R1 structure but with some asymmetry.

412 The winds in the Kelvin wave composites (figures 10c,h) ~~contribute very little to the composite~~  
413 ~~wind~~ are small in magnitude but their composite structures are coherent, with the high-pressure  
414 phase associated with the onshore regime and the low-pressure phase with the offshore regime.  
415 Thus, ~~Kelvin waves may be an indicator of the likely coastal wind regime even though their~~  
416 ~~contribution is too small to be the cause of the coastal wind direction~~ although Kelvin waves are  
417 correlated with the coastal wind, their contribution is small.

418 The analysis of figure 4 in section 3a suggested that, during the field campaign periods, ENSO,  
419 the MJO and equatorial waves all played a role in determining the coastal wind regime. In this  
420 section we have demonstrated the role of these large-scale drivers ~~during 41 DJFs~~ over a longer

421 time period. We now demonstrate that these drivers are sufficient to explain nearly all of the  
422 variability in the coastal wind. As in figure 4, the wind from the identified equatorial waves and  
423 the wind regressed onto ONI and the RMMs were summed, along with the mean seasonal cycle,  
424 and compared to the total field from ERA-Interim. This was carried out for all 421 DJFs (1997/98  
425 to 2017/18) covered by all the contributing data sets; the seasons 1997/98, 1998/99 and 1999/2000  
426 are shown as examples in figure S1. The residual between the grey and ~~solid~~thick black curves was  
427 calculated for each day and a histogram of the absolute value is presented in figure 11. Blue bars  
428 show the number of days in each bin and the orange curve is the cumulative distribution, displayed  
429 as a percentage. The distribution peaks in the lowest bin; a similar histogram (not shown) of the  
430 signed residual (i.e., not the absolute value) is symmetrical about 0, so there is no overall tendency  
431 for the theoretical value to be more onshore or more offshore than the true value.

432 The majority of days have a residual  $< 1.4 \text{ m s}^{-1}$ . The vertical red line is the season-mean  
433 standard deviation in coastal  $u_{850}$ . On 83% of days the residual is less than one standard deviation,  
434 indicating that our theoretical coastal wind reconstructed from the large-scale drivers has a high  
435 degree of accuracy. Inaccuracies may result from inaccuracies in computing the associated wind  
436 for each driver or due to the influence of other drivers such as TCs.

### 437 *c. Extension to other MC coastlines*

438 Sections 3a and 3b investigated the wind regimes on the south-west coast of Sumatra, how they  
439 relate to the diurnal cycle of convection and what large-scale conditions give rise to each regime.  
440 This region was chosen because of the *in situ* data from the pre-YMC and YMC field campaigns,  
441 and ERA5 was used to extend the analysis to gain more robust results. We now use ERA5 to repeat  
442 the analysis over the other MC coastlines in figure 1: north-west Borneo, north Java, south Java  
443 and north New Guinea.

444 Again, ERA5 wind between 1000 hPa and 500 hPa was averaged along the nominal coastline  
445 and the  $k$ -means algorithm was used with  $k = 4$ . For north-west Borneo, as for south-west  
446 Sumatra, zonal wind  $u$  was used; but  $v$  was used for the other three coastlines as they are oriented  
447 approximately east-west. Clusters were again sorted with cluster A being the most onshore and D  
448 the most offshore. Clusters A and D only are shown in figures 12a–h. Values of  $v$  tend to be weaker  
449 than  $u$  so the colour bar shown applies to three of the coastlines only; the north-west Borneo clusters  
450 use the same colour bar as south-west Sumatra (figure 6). Because onshore wind is always plotted  
451 as positive, the north Java and north New Guinea plots show  $-v$ . GPM-HQ composite Hovmöller  
452 diagrams are shown for clusters A and D only in figures 12i–p, with the mean orography plotted  
453 beneath panels (m)–(p).

454 The north-west Borneo clusters are similar to south-west Sumatra, except the mean  $u$  is less  
455 westerly so the onshore cluster is weaker and the offshore cluster is stronger. The associated  
456 precipitation is also similar to Sumatra, with large-scale precipitation dominating in the onshore  
457 regime and organised offshore propagation, preceded by a propagating region of suppression, in  
458 the offshore regime.

459 Since Java is a long, thin island oriented east-west, the winds over the north and south coasts  
460 are very similar (albeit plotted with the opposite sign in figures 12b,f and 12c,g). Thus, north  
461 Java’s strong onshore cluster (A) approximately corresponds to south Java’s offshore cluster (D),  
462 and *vice versa*. The exception is the land-sea breeze within the boundary layer, which is always  
463 anomalously onshore during the day, peaking around 13–14 LT. The same correspondence is seen  
464 in the Hovmöller diagrams in figures 12j,n and 12k,o, remembering that the positive onshore  
465 direction is southward for north Java and northward for south Java. However, the relationship  
466 between wind regime and propagation of convection is different for Java from the Sumatra and  
467 Borneo cases. Java has strong northward propagation (i.e., offshore for the north coast and inland

468 for the south coast) regardless of wind direction (i.e., in both clusters A and D). However, the strong  
469 southward propagation (i.e., inland for the north coast and offshore for the south coast) occurs only  
470 when the wind is from the north (i.e., cluster A for north Java and cluster D for south Java).

471 North New Guinea has a very different coastal wind structure from the other coastlines  
472 investigated here, with all four clusters having onshore wind almost all day in at least the lowest  
473 part of the troposphere (up to around 825 hPa in cluster D; up to around 650 hPa in cluster B; and  
474 over the entire range 1000–500 hPa in clusters A and C, albeit weakly in cluster C). Convection  
475 over New Guinea is strongest on the north and south flanks of the New Guinea Highlands, which  
476 run east-west across the middle of the island and can be seen in the orography cross-section  
477 below figure 12p. The mean altitude along the section is around 2.2 km and the maximum is  
478 around 4.8 km, which is considerably higher than the orography on the other islands studied; and  
479 the mountains are considerably further from the coast (hundreds rather than tens of kilometres).  
480 Convection forms on both flanks of the mountain range regardless of coastal wind cluster, as also  
481 found by Hassim et al. (2016) in convection-permitting simulations. The convection propagates  
482 away from the mountains in both directions, but more strongly on the leeward side.

483 As for south-west Sumatra, we now investigate the large-scale drivers associated with the wind  
484 regimes at each coastline and quantify the extent to which they account for the variability in  
485 clusters (figure 13). The impact of ENSO is weaker over north-west Borneo ( $m_{\text{ONI}}$  from equation 1  
486 is  $-0.74 \text{ m s}^{-1} \text{ }^{\circ}\text{C}^{-1}$  with a correlation of  $\rho = -0.28$ ; figure 13a) than south-west Sumatra ( $m_{\text{ONI}} =$   
487  $-1.38 \text{ m s}^{-1} \text{ }^{\circ}\text{C}^{-1}$  with  $\rho = -0.41$ ; figure 5a). The impact of ENSO over the other three coastlines  
488 is negligible ( $|m_{\text{ONI}}|$  is never larger than  $0.15 \text{ m s}^{-1} \text{ }^{\circ}\text{C}^{-1}$ ; figures 13d,g,j). The impact of the  
489 MJO is also less for north-west Borneo than south-west Sumatra, with the values in figure 13b  
490 around half the magnitude of figure 5b. For the other coastlines (figures 13e,h,k), the values are  
491 small (up to around  $0.7 \text{ m s}^{-1}$ ) compared to the magnitude of the clusters (around  $\pm 3 \text{ m s}^{-1}$ ; see

492 figures 12b–d,f–h), suggesting the MJO also has a limited role in determining the wind regime for  
493 these coastlines. It is notable that the cross-term in equation 2 is very small for south-west Sumatra  
494 and north-west Borneo (the surfaces in figures 5b and 13b and nearly flat) but is much larger for  
495 the other coastlines.

496 Composites of 850 hPa wind anomaly and equatorial waves for clusters A and D are shown for  
497 selected coastlines south Java in figure 14 and north New Guinea in figure 15. Each figure shows the  
498 contributions from R1 (panels (c) and (h)), R2 (panels (d) and (i)) and WMRG (panels (e) and (j))  
499 waves. Equivalent plots for the other coastlines are in the supplementary material – north-west  
500 Borneo (figure S2; Kelvin, R1 and R2 contributions are shown) is very similar to south-west  
501 Sumatra; and north Java (figure S3) is very similar to south Java as discussed below, but for a  
502 change of sign due to being on the opposite coast.

503 For south Java, R1 and WMRG waves both contribute strongly to  $v_{850}$  over the coast, in each  
504 cluster. The strong onshore cluster (A) has the R1 high pressure centres just west of Java so  
505 the eastern edge of the southern hemisphere anti-cyclone contributes positive  $v$  over the coastline  
506 (figure 14c). For the offshore cluster (D), the low pressure centres are just west of Java (figure 14h).  
507 WMRG waves consist of a quadrupole in pressure centred on the equator, with one phase having  
508 high pressure to the south-west and north-east, and low pressure to the north-west and south-east.  
509 This results in a dipole of vorticity, with clockwise rotation to the east and anti-clockwise to the  
510 west. This is the WMRG phase which exists in cluster A (figure 14e), with the vorticity centres  
511 located either side of Java and the two regions of vorticity together contributing positive  $v$  over the  
512 south coast. The opposite phase, with the opposite signs of pressure anomaly and vorticity, is seen  
513 in cluster D (figure 14j).

514 For north New Guinea, by far the greatest contributor to coastal wind is WMRG waves  
515 (figures 15e,j). R1 waves are very weak in the composites for both clusters shown (figures 15c,h),

516 suggesting they do not have a consistent phase in these clusters, so they cancel each other out during  
517 the averaging. R2 waves have much more coherent structures than R1 so, unlike for south-west  
518 Sumatra (see section 3b), there is strong R2 propagation. Like WMRG waves, R2 has a quadrupole  
519 pressure structure but further away from the equator. Centred on the equator are regions of  
520 clockwise and anti-clockwise vorticity, with the western edges of these regions contributing to  $v$   
521 over the coast in clusters A and D (figures 15d,i). In Cluster A, the western edge of a high pressure  
522 region is to the north of New Guinea and a low pressure region to the south; and *vice versa* for  
523 cluster D.

524 In section 3b it was shown that the residual  $u_{850}$  for south-west Sumatra, when calculating the  
525 total wind as the sum of the mean seasonal cycle and the six drivers investigated (ENSO, MJO  
526 and four equatorial waves), is less than one standard deviation on 83% of days (figure 11). The  
527 equivalent histograms for the other coastlines are figures 13c,f,i,l. The percentage of days with  
528 residual less than one standard deviation is 78% for north-west Borneo, 82% for north Java, 83%  
529 for south Java and 79% for north New Guinea. Again, this indicates the large-scale phenomena  
530 investigated can, to a high degree of accuracy, explain the total wind seen over the coastlines  
531 studied, thus exerting a control on the diurnal cycle of convection.

#### 532 **4. Summary and discussion**

533 The MC has a pronounced diurnal cycle of precipitation due to warm oceans and a large number  
534 of islands, with the land-sea temperature contrast creating the conditions for deep convection in the  
535 afternoon and evening as moist air converges over land. On some islands the convection may be  
536 enhanced by significant orography. A weaker diurnal cycle exists over ocean and in some locations  
537 is modified by convection propagating offshore overnight. However, there is a lack of consensus  
538 regarding the mechanism of offshore propagation and its forcing by the large scale. Sources of



539 variability in the diurnal cycle have been investigated in the literature but further understanding is  
540 required, including quantifying the contributions of large-scale controls. This is expected to aid  
541 forecasters in predicting the occurrence of extreme rainfall. Previous work has uncovered scale  
542 interactions with large-scale phenomena such as ENSO, the MJO and equatorial waves, but the  
543 variability of the diurnal cycle within any given phase of these phenomena is still considerable.

544 This study takes a fresh approach to diagnosing the interaction between the diurnal cycle and the  
545 large-scale environment. We take a local-to-large scale approach, rather than the large-to-local scale  
546 technique of producing local composites conditional on the large scale. We use a combination of *in*  
547 *situ* observations, satellite measurements and reanalysis data to investigate these scale interactions.  
548 We test the hypothesis that a range of large-scale drivers exert a control on MC precipitation through  
549 their modulation of the coastal wind regimes, and quantify the relative contributions of each driver.

550 The *k*-means clustering algorithm is used to define the coastal wind regimes, first using 108 days  
551 of field campaign radiosonde data on the coast of Sumatra before extending the analysis using  
552 ERA5 to 41 DJFs and the other coastlines labelled in figure 1. For most coastlines, the regime with  
553 strong onshore winds all day has suppressed convection over land and an active region of convection  
554 over the sea, with a lower than average probability of extreme rainfall (above the 99<sup>th</sup> percentile)  
555 occurring. The regime with predominantly offshore winds produces the canonical diurnal cycle  
556 with strong convection over the land, a higher than average probability of extreme rainfall, and  
557 propagation offshore overnight. This is consistent with Yokoi et al. (2019) who showed, also  
558 using the pre-YMC and YMC observations, that around 800 hPa the wind is more offshore from  
559 south-west Sumatra on days with offshore propagation than on days without.

560 The 850 hPa wind anomaly associated with ENSO, the MJO and convectively-coupled equatorial  
561 waves was computed at each coastline, and used to quantify the contribution of each of these drivers  
562 to the coastal wind regime. The sum of these contributions explains the total wind to a high degree

563 of accuracy, with the residual value having an amplitude smaller than one standard deviation on  
564 78% and 83% of days. Remaining discrepancies are likely due to deficiencies in the technique  
565 for deriving the wind associated with each driver, or the influence of other drivers such as TCs,  
566 tropical depressions, cold surges, Borneo vortices or the Indian Ocean dipole. Composites of  
567 large-scale conditions with large residuals (not shown) suggest that the largest inaccuracies tend to  
568 be associated with either active phases of the MJO or R1 waves.

569 It is important to note that studies such as Peatman et al. (2014), which show the mean diurnal  
570 cycle of precipitation for each MJO phase, do not necessarily imply that the diurnal cycle plotted  
571 will always occur on days in that phase. Rather, the results of such papers are true only in a  
572 composite sense. MJO phase alone does not determine the small-scale weather regime and it  
573 cannot be used to predict the local distribution of thunderstorms on an individual day. Instead, a  
574 combination of large-scale phenomena, which may occur in any combination, should be considered.

575 Figure 16 summarises the drivers contributing to the onshore and offshore wind regimes for each  
576 coastline, with details of which phase of the large-scale phenomenon contributes to each cluster.  
577 Drivers are listed if the [1997/98 to 2017/18 DJF](#) variance in their associated coastal 850 hPa wind  
578 [\(see figure S1 for the first three years\)](#) exceeds 10% of the variance of the total value, for each  
579 coastline (all variances are listed in table S4). The schematic diagrams in figure 17 indicate how  
580 these drivers affect coastal wind and show the associated variability in precipitation. Cumulonimbus  
581 clouds indicate deep convection and cumulus clouds indicate less intense precipitation. Grey arrows  
582 indicate propagation of convection, with the strength of propagation shown by the arrow size.

583 For south-west Sumatra there is a strong contribution from Rossby waves. Deep convection  
584 over the mountains and nocturnal offshore propagation are more likely during the high pressure  
585 phase of the R1 wave. The stronger high pressure signal is in the southern hemisphere because the  
586 coastline is in that hemisphere. When there is some asymmetry in the Rossby wave signal there is

587 also some projection onto the R2 structure. Therefore, the two wave types are considered together  
588 in the top row of figure 16 and the asymmetry is illustrated in figure 17e. The opposite phase, with  
589 low pressure centres, is associated with more moderate, large-scale precipitation which propagates  
590 onshore (figure 17a). The same result is found for north-west Borneo (figures 17b,f), but with  
591 the stronger signals in the northern hemisphere because the coastline investigated is north of the  
592 equator.

593 The MJO and ENSO also contribute to the coastal wind for south-west Sumatra. The enhanced  
594 diurnal cycle is most often found in phases prior to the arrival of the active MJO envelope (8–3),  
595 consistent with Oh et al. (2012), Peatman et al. (2014) and other studies, when the wind is more  
596 offshore. The diurnal cycle is more suppressed during phases 4 to 6. El Niño is associated with  
597 offshore wind, consistent with large-scale suppression and low-level divergence over the region;  
598 and is therefore associated with an enhanced diurnal cycle, consistent with Rauniyar and Walsh  
599 (2013). The effect of ENSO is weaker over north-west Borneo than south-west Sumatra, possibly  
600 because the ENSO wind signal is due to large-scale convergence or divergence at the edge of the  
601 MC region. However, north-west Borneo does have a contribution from the MJO, with onshore  
602 and offshore wind regimes tending to occur one phase later than over south-west Sumatra due to  
603 the longitudinal difference.

604 Over Java and north New Guinea, where the coastal wind we consider is meridional, there is  
605 no substantial contribution from ENSO or the MJO, which is consistent with the fact that both  
606 these phenomena are associated with anomalies in a zonal overturning circulation. Variability in  
607 coastal wind regimes instead arises from the propagation of Rossby and WMRG waves. Since  
608 Java is a thin island in the north-south direction, onshore wind on the north coast often coincides  
609 with offshore wind on the south coast, and *vice versa*. The control of large-scale drivers on the  
610 coastal wind regimes is, therefore, roughly the same at each coastline but for a change of sign in

611 wind direction (see yellow and blue rows of figure 16) so only south Java is shown in figure 17  
612 (panels (c) and (g)). Rossby waves projecting onto R1 and R2 again have a strong contribution over  
613 Java, as do WMRG waves. Deep convection occurs over the Java mountains in both the onshore  
614 and offshore wind regimes, with northward propagation occurring in both. Southward propagation  
615 also occurs in both regimes but is considerably stronger when winds are offshore from the south  
616 coast.

617 Over north New Guinea, WMRG waves have the greatest contribution to coastal wind. Although  
618 the variance in coastal wind due to R1 waves is 14.9% of the variance in the total coastal wind,  
619 composites do not show a coherent signal (figures 15c,h) so there is no consistent phase of the wave  
620 associated with a given wind regime. Therefore, we do not provide information about the phase of  
621 these waves in figure 16 and we omit them from figures 17d,h. However, there is a coherent signal  
622 for R2 waves. The R2 structure has high and low pressure centres located away from the equator,  
623 and vorticity centred on the equator, as indicated in figures 17d,h. It is these equatorial vorticity  
624 centres which contribute to wind on the north New Guinea coast.

625 The New Guinea highlands are higher and broader than most of the orography in other MC  
626 regions studied in this paper (see figure 1). Unlike on other islands, there are two distinct regions  
627 of convective initiation, on the north and south flanks of the mountain range. As shown by the  
628 schematic diagram and as was seen in the Hovmöller diagrams in figures 12l,p, the most intense  
629 precipitation forms on the leeward side of the mountains. In both regimes the convection on the  
630 north side propagates northwards and on the south side propagates southwards, with the strongest  
631 propagation arising from the more intense convection.

632 The stark differences in the results for Java and north New Guinea, compared with south-west  
633 Sumatra and north-west Borneo, demonstrate the diversity in the behaviour of the diurnal cycle

634 across the MC. More work is required to understand the differences in the underlying physical  
635 mechanisms occurring in each location.

636 In summary, we have shown that the strength and absolute wind direction within the coastal  
637 land-sea breeze circulation exerts a strong control on the diurnal convection and offshore  
638 propagation over MC coastlines. Our local-to-large scale method, using a clustering algorithm, is a  
639 powerful tool which has allowed us to identify what large-scale conditions set up each local regime.  
640 The summary information in figure 16 and figure 17 have applications for forecasting in the region.  
641 Global NWP models struggle to forecast the local-scale spatial and temporal distribution of rainfall  
642 accurately in the tropics, at least partly due to errors in convection parametrization schemes (e.g.,  
643 Birch et al. 2015; Argüeso et al. 2020). However, large-scale drivers can be forecast skilfully  
644 several days or weeks in advance. For example, operational forecasting systems may skilfully  
645 predict the MJO on time scales of 3–4 weeks (e.g., Klingaman and Woolnough 2014; Kim et al.  
646 2014); and Rossby and WMRG waves on time scales of around 1 week (e.g., Yang et al. 2021). Our  
647 results allow forecasters to harness such skill through understanding the impact of the large-scale  
648 environment and suggest there may be opportunities to infer the risk of high-impact weather from  
649 predicted large-scale weather regimes (cf. Neal et al. 2016, 2020). This information can be used  
650 alongside NWP forecasts to improve prediction of extreme rainfall.

651 *Acknowledgments.* This work is part of the Vertical Structure of Weather project, funded by the  
652 Met Office Weather and Climate Science for Service Partnership (WCSSP) Southeast Asia, as  
653 part of the Newton Fund; and the TerraMaris project, funded by National Environment Research  
654 Council (NERC) grant NE/R016739/1. The “pre-YMC” and “YMC” field campaign data were  
655 collected as part of YMC, led by investigator Dr Kunio Yoneyama. The equatorial wave data set  
656 was produced as part of the Newton Fund project under the auspices of the WCSSP Southeast

657 Asia project by Dr Gui-Ying Yang of the National Centre for Atmospheric Science, University  
658 of Reading. Data analysis and plots used the Iris Python package for Earth science data, version  
659 2.4.0 (Met Office 2020). *k*-means clustering and multiple linear regression were performed using  
660 the Scikit-learn Python package for machine learning, version 0.22.1 (Pedregosa et al. 2011).  
661 The authors are grateful to Dr Steve Woolnough for providing Python code for filtering data in  
662 wavenumber-frequency space. [The authors would like to thank three anonymous reviewers for  
663 their comments on this paper.](#)

664 *Data availability statement.* The “pre-YMC” and “YMC” field campaign data are archived by the  
665 Japan Agency for Marine-Earth Science and Technology (JASMTEC) at [http://www.jamstec.  
666 go.jp/ymc/ymc\\_data.html](http://www.jamstec.go.jp/ymc/ymc_data.html).

## 667 **References**

668 Argüeso, D., R. Romero, and V. Homar, 2020: Precipitation features of the Maritime Continent in  
669 parameterized and explicit convection models. *Journal of Climate*, **33** (6), 2449–2466, doi:10.  
670 1175/JCLI-D-19-0416.1.

671 Baranowski, D. B., M. K. Flatau, P. J. Flatau, and A. J. Matthews, 2016: Impact of  
672 atmospheric convectively coupled equatorial Kelvin waves on upper ocean variability: AIR-SEA  
673 INTERACTIONS IN CCKWS. *Journal of Geophysical Research: Atmospheres*, **121** (5),  
674 2045–2059, doi:10.1002/2015JD024150.

675 Birch, C. E., M. J. Roberts, L. Garcia-Carreras, D. Ackerley, M. J. Reeder, A. P. Lock,  
676 and R. Schiemann, 2015: Sea-breeze dynamics and convection initiation: The influence of  
677 convective parameterization in weather and climate model biases. *Journal of Climate*, **28** (20),  
678 8093–8108, doi:10.1175/JCLI-D-14-00850.1.

679 Birch, C. E., S. Webster, S. C. Peatman, D. J. Parker, A. J. Matthews, Y. Li, and M. E. E. Hassim,  
680 2016: Scale interactions between the MJO and the western Maritime Continent. *Journal of*  
681 *Climate*, **29** (7), 2471–2492, doi:10.1175/JCLI-D-15-0557.1.

682 Climate Prediction Center, 2020: Oceanic Niño Index. URL [https://origin.cpc.ncep.noaa.gov/](https://origin.cpc.ncep.noaa.gov/products/analysis_monitoring/ensostuff/ONI_v5.php)  
683 [products/analysis\\_monitoring/ensostuff/ONI\\_v5.php](https://origin.cpc.ncep.noaa.gov/products/analysis_monitoring/ensostuff/ONI_v5.php).

684 Dee, D. P., and Coauthors, 2011: The ERA-Interim reanalysis: configuration and performance  
685 of the data assimilation system. *Quarterly Journal of the Royal Meteorological Society*, **137**,  
686 553–597, doi:10.1002/qj.828.

687 Ferrett, S., G.-Y. Yang, S. J. Woolnough, J. Methven, K. Hodges, and C. E. Holloway, 2020:  
688 Linking extreme precipitation in Southeast Asia to equatorial waves. *Quarterly Journal of the*  
689 *Royal Meteorological Society*, **146** (727), 665–684, doi:10.1002/qj.3699.

690 Gelaro, R., and Coauthors, 2017: The Modern-Era Retrospective analysis for Research and  
691 Applications, version 2 (MERRA-2). *Journal of Climate*, **30** (14), 5419–5454, doi:10.1175/  
692 JCLI-D-16-0758.1.

693 Hassim, M. E. E., T. P. Lane, and W. W. Grabowski, 2016: The diurnal cycle of rainfall over New  
694 Guinea in convection-permitting WRF simulations. *Atmospheric Chemistry and Physics*, **16** (1),  
695 161–175, doi:10.5194/acp-16-161-2016.

696 Heale, C. J., J. B. Snively, A. N. Bhatt, L. Hoffmann, C. C. Stephan, and E. A. Kendall, 2019:  
697 Multilayer Observations and Modeling of Thunderstorm-Generated Gravity Waves Over the  
698 Midwestern United States. *Geophysical Research Letters*, doi:10.1029/2019GL085934.

699 Hersbach, H., and Coauthors, 2020: The ERA5 global reanalysis. *Quarterly Journal of the Royal*  
700 *Meteorological Society*, **146** (730), 1999–2049, doi:10.1002/qj.3803.

701 Houze, R. A., S. G. Geotis, F. D. Marks, and A. K. West, 1981: Winter monsoon convection  
702 in the vicinity of north Borneo. Part I: Structure and time variation of the clouds and  
703 precipitation. *Monthly Weather Review*, **109** (8), 1595–1614, doi:10.1175/1520-0493(1981)  
704 109<1595:WMCITV>2.0.CO;2.

705 Kim, H.-M., P. J. Webster, V. E. Toma, and D. Kim, 2014: Predictability and prediction skill  
706 of the MJO in two operational forecasting systems. *Journal of Climate*, **27** (14), 5364–5378,  
707 doi:10.1175/JCLI-D-13-00480.1.

708 Klingaman, N. P., and S. J. Woolnough, 2014: Using a case-study approach to improve  
709 the Madden-Julian oscillation in the Hadley Centre model. *Quarterly Journal of the Royal*  
710 *Meteorological Society*, **140** (685), 2491–2505, doi:10.1002/qj.2314.

711 Knapp, K. R., M. C. Kruk, D. H. Levinson, H. J. Diamond, and C. J. Neumann, 2010: The  
712 International Best Track Archive for Climate Stewardship (IBTrACS) project: Unifying tropical  
713 cyclone data. *Bulletin of the American Meteorological Society*, **91**, 363–376, doi:10.1175/  
714 2009BAMS2755.1.

715 Love, B. S., A. J. Matthews, and G. M. S. Lister, 2011: The diurnal cycle of precipitation over  
716 the Maritime Continent in a high-resolution atmospheric model. *Quarterly Journal of the Royal*  
717 *Meteorological Society*, **137**, 934–947, doi:10.1002/qj.809.

718 Lubis, S. W., and M. R. Respati, 2021: Impacts of convectively coupled equatorial waves on rainfall  
719 extremes in Java, Indonesia. *International Journal of Climatology*, doi:10.1002/joc.6967.

720 MacQueen, J., 1967: Some methods for classification and analysis of multivariate observations.  
721 *Proceedings of the Fifth Berkeley Symposium on Mathematical Statistics and Probability:*  
722 *Volume I: Theory of Statistics*, 281–297.



723 Madden, R. A., and P. R. Julian, 1971: Detection of a 40-50 day oscillation in the zonal wind  
724 in the tropical Pacific. *Journal of the Atmospheric Sciences*, **28** (5), 702–708, doi:10.1175/  
725 1520-0469(1971)028<0702:DOADOI>2.0.CO;2.

726 Madden, R. A., and P. R. Julian, 1972: Description of global-scale circulation cells in the tropics  
727 with a 40-50 day period. *Journal of the Atmospheric Sciences*, **29** (6), 1109–1123, doi:10.1175/  
728 1520-0469(1972)029<1109:DOGSCC>2.0.CO;2.

729 Mapes, B. E., T. T. Warner, and M. Xu, 2003: Diurnal patterns of rainfall in northwestern South  
730 America. Part III: Diurnal gravity waves and nocturnal convection offshore. *Monthly Weather*  
731 *Review*, **131** (5), 830–844, doi:10.1175/1520-0493(2003)131<0830:DPORIN>2.0.CO;2.

732 Matthews, A. J., 2000: Propagation mechanisms for the Madden-Julian Oscillation. *Quarterly*  
733 *Journal of the Royal Meteorological Society*, **126** (569), 2637–2651, doi:10.1002/qj.  
734 49712656902.

735 Met Office, 2020: Iris: A Python library for analysing and visualising meteorological and  
736 oceanographic data sets. <http://scitools.org.uk>.

737 Mohd Nor, M. F. F., C. E. Holloway, and P. M. Inness, 2020: The role of local orography on the  
738 development of a severe rainfall event over western peninsular Malaysia: A case study. *Monthly*  
739 *Weather Review*, **148** (5), 2191–2209, doi:10.1175/MWR-D-18-0413.1.

740 Mori, S., H. Jun-Ichi, Y. I. Tauhid, and M. D. Yamanaka, 2004: Diurnal land-sea rainfall peak  
741 migration over Sumatera Island, Indonesian Maritime Continent, observed by TRMM satellite  
742 and intensive rawinsonde soundings. *Monthly Weather Review*, **132** (8), 2021–2039, doi:10.  
743 1175/1520-0493(2004)132<2021:DLRPMO>2.0.CO;2.

- 744 Muhammad, F. R., S. W. Lubis, and S. Setiawan, 2021: Impacts of the Madden-Julian Oscillation on  
745 precipitation extremes in Indonesia. *International Journal of Climatology*, doi:10.1002/joc.6941.
- 746 Neal, R., D. Fereday, R. Crocker, and R. E. Comer, 2016: A flexible approach to defining weather  
747 patterns and their application in weather forecasting over Europe. *Meteorological Applications*,  
748 **23 (3)**, 389–400, doi:/10.1002/met.1563.
- 749 Neal, R., J. Robbins, R. Dankers, A. Mitra, A. Jayakumar, E. N. Rajagopal, and G. Adamson, 2020:  
750 Deriving optimal weather pattern definitions for the representation of precipitation variability  
751 over India. *International Journal of Climatology*, **40 (1)**, 342–360, doi:/10.1002/joc.6215.
- 752 Oh, J. H., K. Y. Kim, and G. H. Lim, 2012: Impact of MJO on the diurnal cycle of rainfall over the  
753 western Maritime Continent in the austral summer. *Climate Dynamics*, **38 (5–6)**, 1167–1180,  
754 doi:10.1007/s00382-011-1237-4.
- 755 Peatman, S. C., A. J. Matthews, and D. P. Stevens, 2014: Propagation of the Madden-Julian  
756 Oscillation through the Maritime Continent and scale interaction with the diurnal cycle of  
757 precipitation. *Quarterly Journal of the Royal Meteorological Society*, **140 (680)**, 814–825,  
758 doi:10.1002/qj.2161.
- 759 Pedregosa, F., and Coauthors, 2011: Scikit-learn: Machine Learning in Python. *Journal of Machine*  
760 *Learning Research*, **12 (85)**, 2825–2830.
- 761 Qian, J.-H., 2008: Why precipitation is mostly concentrated over islands in the Maritime Continent.  
762 *Journal of the Atmospheric Sciences*, **65 (4)**, 1428–1441, doi:10.1175/2007JAS2422.1.
- 763 Qian, J.-H., 2020: Mechanisms for the dipolar patterns of rainfall variability over large islands in the  
764 Maritime Continent associated with the Madden-Julian Oscillation. *Journal of the Atmospheric*  
765 *Sciences*, **77 (6)**, 2257–2278, doi:10.1175/JAS-D-19-0091.1.

766 Ramage, C. S., 1968: Role of a Tropical “Maritime Continent” in the atmospheric  
767 circulation. *Monthly Weather Review*, **96** (6), 365–370, doi:10.1175/1520-0493(1968)  
768 096<0365:ROATMC>2.0.CO;2.

769 Rauniar, S. P., and K. J. E. Walsh, 2011: Scale interaction of the diurnal cycle of rainfall over the  
770 Maritime Continent and Australia: Influence of the MJO. *Journal of Climate*, **24** (2), 325–348,  
771 doi:10.1175/2010JCLI3673.1.

772 Rauniar, S. P., and K. J. E. Walsh, 2013: Influence of ENSO on the diurnal cycle of rainfall  
773 over the Maritime Continent and Australia. *Journal of Climate*, **26** (4), 1304–1321, doi:10.1175/  
774 JCLI-D-12-00124.1.

775 Sakaeda, N., G. Kiladis, and J. Dias, 2020: The diurnal cycle of rainfall and the convectively  
776 coupled equatorial waves over the Maritime Continent. *Journal of Climate*, **33** (8), 3307–3331,  
777 doi:10.1175/JCLI-D-19-0043.1.

778 Vincent, C. L., and T. P. Lane, 2016: Evolution of the diurnal precipitation cycle with the passage  
779 of a Madden-Julian Oscillation event through the Maritime Continent. *Monthly Weather Review*,  
780 **144** (5), 1983–2005, doi:10.1175/MWR-D-15-0326.1.

781 Warner, T. T., B. E. Mapes, and M. Xu, 2003: Diurnal patterns of rainfall in northwestern South  
782 America. Part II: Model simulations. *Monthly Weather Review*, **131** (5), 813–829, doi:10.1175/  
783 1520-0493(2003)131<0813:DPORIN>2.0.CO;2.

784 Wheeler, M. C., and H. H. Hendon, 2004: An all-season real-time multivariate MJO index:  
785 Development of an index for monitoring and prediction. *Monthly Weather Review*, **132**,  
786 1917–1932, doi:10.1175/1520-0493(2004)132<1917:AARMMI>2.0.CO;2.

- 787 Wu, P., M. Hara, J.-i. Hamada, M. D. Yamanaka, and F. Kimura, 2009: Why a large amount of rain  
788 falls over the sea in the vicinity of western Sumatra Island during nighttime. *Journal of Applied*  
789 *Meteorology and Climatology*, **48 (7)**, 1345–1361, doi:10.1175/2009JAMC2052.1.
- 790 Xavier, P., R. Rahmat, W. K. Cheong, and E. Wallace, 2014: Influence of Madden-Julian Oscillation  
791 on Southeast Asia rainfall extremes: Observations and predictability. *Geophysical Research*  
792 *Letters*, **41 (12)**, 4406–4412, doi:10.1002/2014GL060241.
- 793 Yang, G.-Y., S. Ferrett, S. Woolnough, J. Methven, and C. Holloway, 2021: Real-time identification  
794 of equatorial waves and evaluation of waves in global forecasts. *Weather and Forecasting*, **36 (1)**,  
795 171–193, doi:10.1175/WAF-D-20-0144.1.
- 796 Yang, G.-Y., B. J. Hoskins, and J. M. Slingo, 2003: Convectively coupled equatorial waves: A new  
797 methodology for identifying wave structures in observational data. *Journal of the Atmospheric*  
798 *Sciences*, **60 (14)**, 1637–1654, doi:10.1175/1520-0469(2003)060<1637:CCEWAN>2.0.CO;2.
- 799 Yokoi, S., S. Mori, F. Syamsudin, U. Haryoko, and B. Geng, 2019: Environmental conditions for  
800 nighttime offshore migration of precipitation area as revealed by in situ observation off Sumatra  
801 Island. *Monthly Weather Review*, **147 (9)**, 3391–3407, doi:10.1175/MWR-D-18-0412.1.
- 802 Yoneyama, K., and C. Zhang, 2020: Years of the Maritime Continent. *Geophysical Research*  
803 *Letters*, **47 (12)**, e2020GL087182, doi:10.1029/2020GL087182.

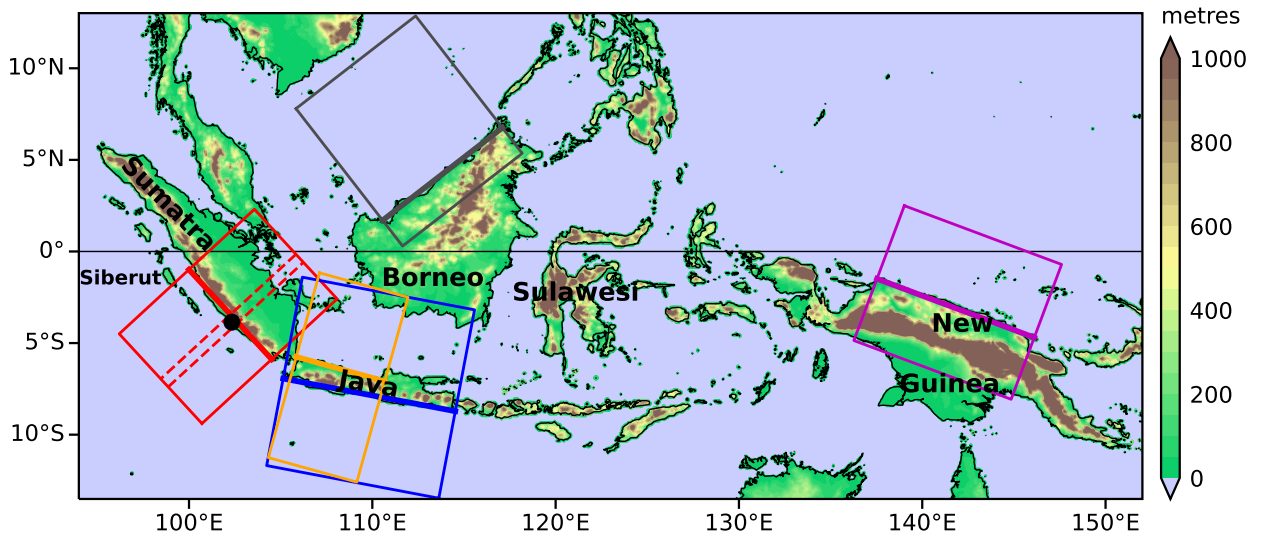
## LIST OF FIGURES

804		
805	<b>Fig. 1.</b>	Orography of the MC with selected islands labelled. Solid boxes indicate rotated grids used in the analysis, with the internal thick line indicating the nominal coastline, for south-west Sumatra (red), north-west Borneo (grey), north Java (orange), south Java (blue) and north New Guinea (magenta). The red dashed box is used instead of the solid box when analysing data from the field campaigns at Bengkulu. Bengkulu is shown by the black dot inside the dashed box. . . . . 40
811	<b>Fig. 2.</b>	(a–c) Diurnal cycle of vertical profile of zonal wind from radiosondes at Bengkulu during the 108 days 2015/09/11–2015/12/25 and 2017/11/16–2018/01/15. Days are sorted into 3 clusters using the $k$ -means algorithm (see main text for details), with the number of days in each cluster shown above each panel. Clusters are ordered according to the mean value of zonal wind averaged over time and pressure. Radiosonde data are every 3 hours and interpolated to the same pressure levels used by the ERA5 reanalysis, from 1000 to 500 hPa, as indicated by the tick marks. Local time is taken to be UTC+7. (d–f) As (a–c) but plotted as a diurnal anomaly; that is, with the respective daily mean profile for each cluster subtracted. . . . . 41
819	<b>Fig. 3.</b>	Hovmöller diagrams of the composite diurnal cycle of precipitation from IMERG for each of the clusters in figure 2, extended by 12 hours to 19 LT (12 UTC) the following day. Precipitation is composited over the red dashed box in figure 1 and averaged along the coastline, every 30 minutes. The mean orography is shown below each panel in metres above sea level (ASL). . . . . 42
824	<b>Fig. 4.</b>	Time series of $u_{850}$ (grey) from ERA-Interim at Bengkulu during the two field campaigns. Coloured curves show $u'_{850}$ due to ENSO (dark green; regression onto ONI), the MJO (dark blue; multiple regression onto RMMs), equatorial Kelvin (orange), R1 (dark pink), R2 (light pink) and WMRG (light blue) waves (identified in ERA-Interim). Thin black dotted curve shows the mean seasonal cycle. Thick black solid curve is the sum of the six coloured curves and the mean seasonal cycle. Red stars indicate a TC centre within $10^\circ$ geodesic of Bengkulu. (All TCs shown are in the southern hemisphere.) Red, green and blue boxes denote clusters from figures 2a–c. . . . . 43
832	<b>Fig. 5.</b>	(a) Linear regression of south-west Sumatra coast $u'_{850}$ onto ONI index of ENSO, according to equation 1. The data points used for the regression are shown in grey. $\rho$ is the correlation coefficient. (b) Multiple linear regression of south-west Sumatra coast $u'_{850}$ onto RMM indices of the MJO, according to equation 2. Areas with no MJO days in the 39 DJFs used are greyed out. . . . . 44
837	<b>Fig. 6.</b>	(a–d) Hourly ERA5 zonal wind averaged along the nominal coastline of the solid red box (south-west Sumatra) in figure 1, clustered using the $k$ -means algorithm. 41 DJFs (1979/80–2019/20, excluding 29 February) are used with $k = 4$ (see main text for details of the choice of $k$ ) and clusters labelled A, B, C and D to avoid confusion with the $k = 3$ clustering in figure 2. (e–h) As (a–d) but plotted as a diurnal anomaly; that is, with the respective daily mean profile for each cluster subtracted. . . . . 45
843	<b>Fig. 7.</b>	Hovmöller diagrams of the composite diurnal cycle of precipitation from GPM-HQ for each of the clusters in figure 6. These composites use a subset (20 DJFs) of the days in figure 6 as GPM is not available before the year 2000. . . . . 46
846	<b>Fig. 8.</b>	Fractional change (expressed as a percentage), relative to climatology, of the probability of extreme precipitation occurring in each cluster, using daily mean IMERG-GPM-HQ rainfall for the 20 DJFs from 2000/01 onwards. Extreme precipitation is defined as exceeding the

849	99 <sup>th</sup> percentile, so the climatological probability is 0.01 everywhere. Data are regridded to	
850	0.25° for plotting purposes. . . . .	47
851	<b>Fig. 9.</b> (a) Number of days in DJFs 1979/80–2019/20 in each phase of ENSO. (b) As (a) but	
852	separately for each of the clusters in figure 6. (c,d) As (a,b) but for the MJO, with grey	
853	indicating RMM amplitude < 1. MJO large-scale convection is active over the Indian Ocean	
854	in phases 2–3, the MC in 4–5, the western Pacific Ocean in 6–7, and the western hemisphere	
855	and Africa in 8–1; and is suppressed in the corresponding opposite phases. . . . .	48
856	<b>Fig. 10.</b> Composites at 850 hPa for clusters A and D from figures 6a,d. (a,f) Daily mean horizontal	
857	wind anomaly using ERA-Interim reanalysis data. (b,g) Daily mean horizontal wind and	
858	geopotential height anomalies from structures of equatorial waves, summed over Kelvin, R1,	
859	R2 and WMRG waves. (c,h) As (b,g) but for Kelvin wave contribution only. (d,i) As (b,g)	
860	but for R1 wave contribution only. (e,j) As (b,g) but for R2 wave contribution only. All	
861	composites use a subset (21 DJFs) of the days in figure 6, for 1997/98 to 2017/18. . . . .	49
862	<b>Fig. 11.</b> Histogram of the absolute value of the residual south-west Sumatra coast $u_{850}$ , with the	
863	theoretical value computed as the sum of the contributions from the MJO, ENSO, equatorial	
864	Kelvin, R1, R2 and WMRG waves, and the mean seasonal cycle. For the example days	
865	shown in figures 4 and S1, this is the absolute difference between the grey and <b>solidthick</b>	
866	black curves. Blue bars show the number of days in each bin (left vertical axis); orange curve	
867	shows the cumulative distribution as a percentage (right vertical axis); and red line shows	
868	the inter-annual standard deviation of $u_{850}$ , averaged over each day of DJF. . . . .	50
869	<b>Fig. 12.</b> (a–h) As figure 6 but extended to the other coastlines shown in figure 1, for $k = 4$ (clusters B	
870	and C not shown). $u$ and $v$ after each coastline name indicate whether zonal or meridional	
871	wind was clustered. Wind in the onshore direction is plotted in red and the offshore direction	
872	in blue, with cluster A as the most onshore cluster. For north Java and north New Guinea this	
873	requires the sign to be reversed so $-v$ is plotted. Note that panels (a) and (e) use the same	
874	colour bar (not shown here) as figure 6. (i–p) As figure 7 but for the clusters shown here in	
875	panels a–h. . . . .	51
876	<b>Fig. 13.</b> Top two rows as figure 5 and bottom row as figure 11, but for (a–c) north-west Borneo,	
877	(d–f) north Java, (g–i) south Java and (j–l) north New Guinea. For middle row, colours are	
878	chosen so that red is always onshore wind. For bottom row, tick marks up to 600 (number of	
879	days in each bin; left axis) relate to blue bars; and horizontal grid lines and tick marks up to	
880	100 (cumulative distribution as a percentage; right axis) relate to orange curves. . . . .	52
881	<b>Fig. 14.</b> (a,b,f,g) As figure 10 but for south Java clusters A and D (see figures 12c,g). (c,h) R1,	
882	(d,i) R2 and (e,j) WMRG contributions only. . . . .	53
883	<b>Fig. 15.</b> As figure 14 but for north New Guinea clusters A and D (see figures 12d,h). . . . .	54
884	<b>Fig. 16.</b> Summary of the large-scale drivers with the strongest control on coastal wind regime, and the	
885	phases associated with the strongest onshore and offshore regimes, for each of the coastlines	
886	analysed. Forcings are listed if the variance in their associated $u'_{850}$ or $v'_{850}$ (depending on	
887	the coastline) is at least 10% of the variance in the full $u_{850}$ or $v_{850}$ field <b>during DJFs 1997/98</b>	
888	<b>to 2017/18</b> ; for a full list, see table S4. Colours correspond to the boxes in figure 1, with	
889	more intense shades highlighting larger contributions to the variability. *For coastlines other	
890	than north New Guinea, identified R2 waves appear to be an artefact of the same circulation	
891	pattern which projects more strongly onto the theoretical R1 structure, so the two are shown	
892	in combination. **For north New Guinea, although the variance associated with R1 waves	

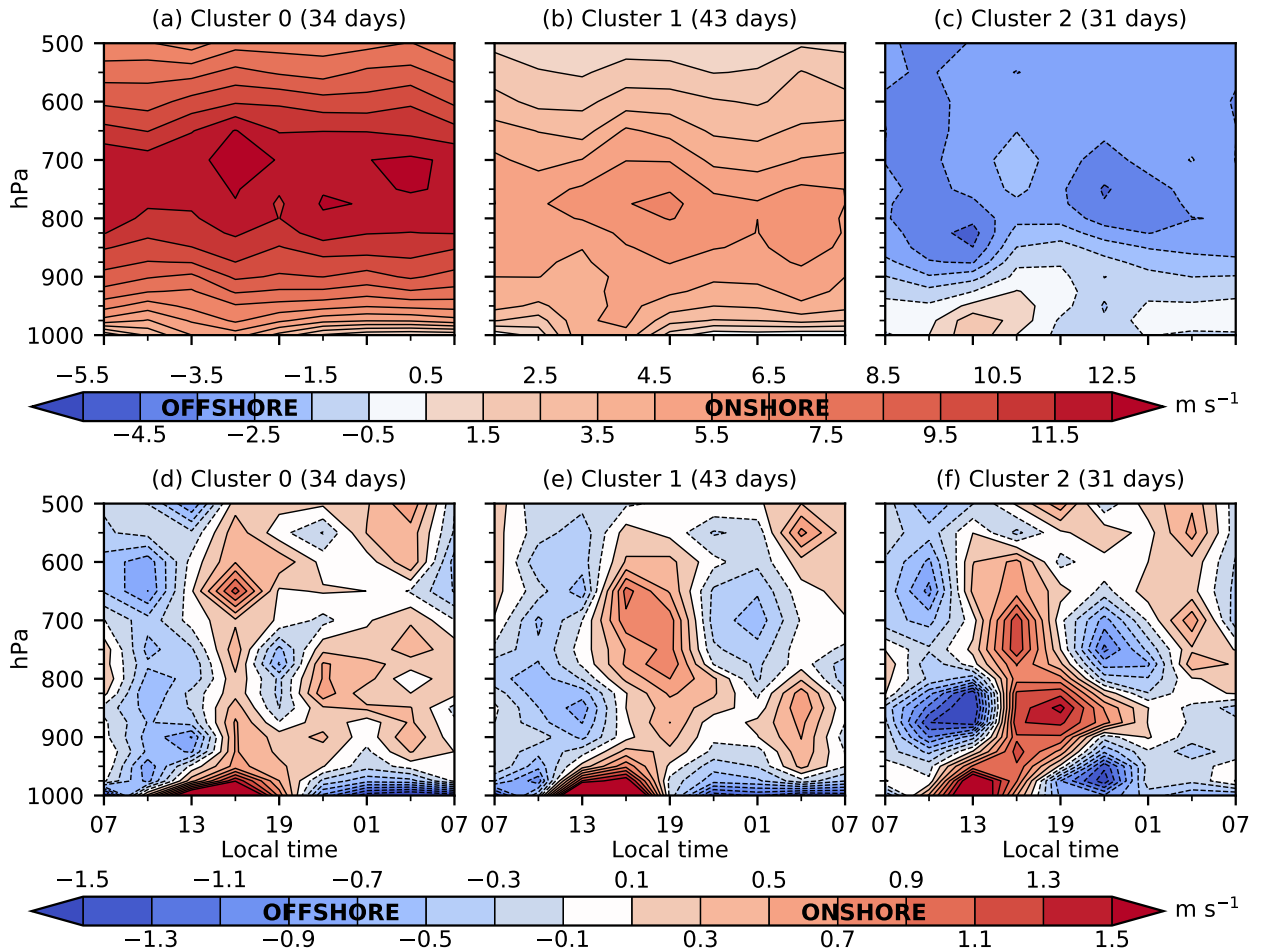
893 is high enough to be listed here, their phase is not consistent within each cluster and their  
894 contribution to coastal  $v_{850}$  is weak in a composite sense (see figures 15c,h). . . . . 55

895 **Fig. 17.** Schematic diagram of important large-scale drivers, and their effect on convection and its  
896 propagation, for strong onshore and offshore coastal wind regimes for the Maritime Continent  
897 coastlines detailed in figure 16. North Java is not shown due to its similarity to the results for  
898 south Java (with onshore and offshore reversed). Dark grey cumulonimbus clouds indicate  
899 intense convection and rainfall; light grey cumulus clouds indicate more moderate rainfall.  
900 Grey arrows indicate propagation, with the largest arrow in an image indicating the strongest  
901 propagation (not to scale between images). These are drawn with reference to the Hovmöller  
902 diagrams in figures 7 and 12i–p. Coloured arrows indicate the wind direction associated  
903 with large-scale drivers. H and L refer to high and low pressure centres. For  $n = 1, 2$  Rossby  
904 waves these differ in size between hemispheres (see main text for details). MJO numbers  
905 refer to phases from Wheeler and Hendon (2004). The dashed line marks the equator. Major  
906 mountains are shown for each island (relative size between images not to scale). . . . . 56

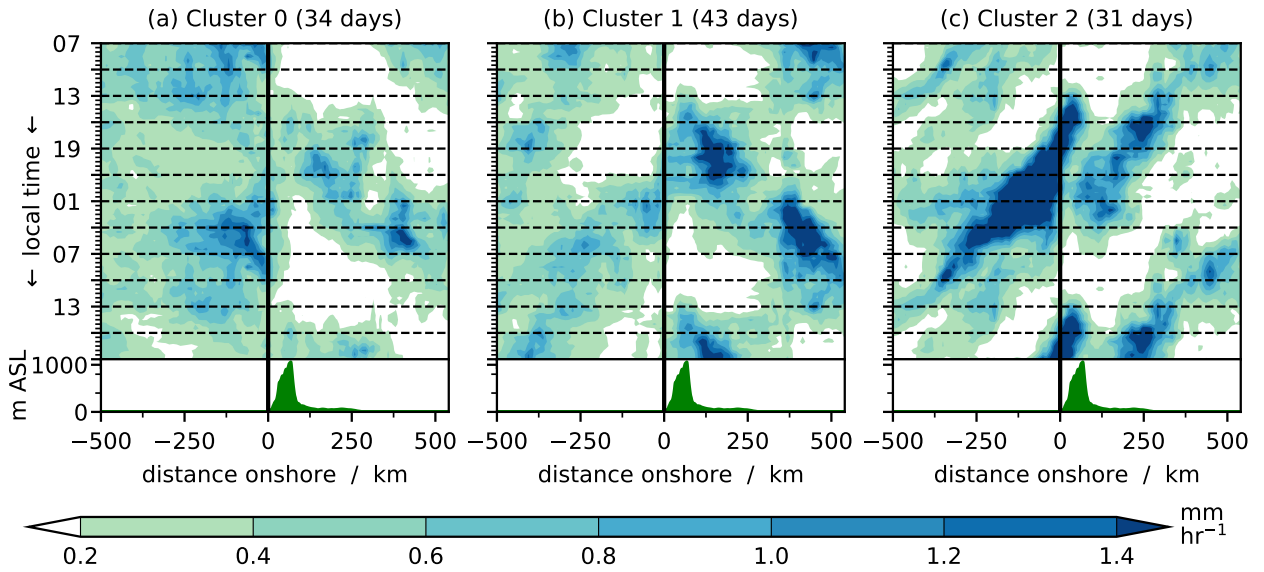


907 FIG. 1. Orography of the MC with selected islands labelled. Solid boxes indicate rotated grids used in the  
 908 analysis, with the internal thick line indicating the nominal coastline, for south-west Sumatra (red), north-west  
 909 Borneo (grey), north Java (orange), south Java (blue) and north New Guinea (magenta). The red dashed box is  
 910 used instead of the solid box when analysing data from the field campaigns at Bengkulu. Bengkulu is shown by  
 911 the black dot inside the dashed box.

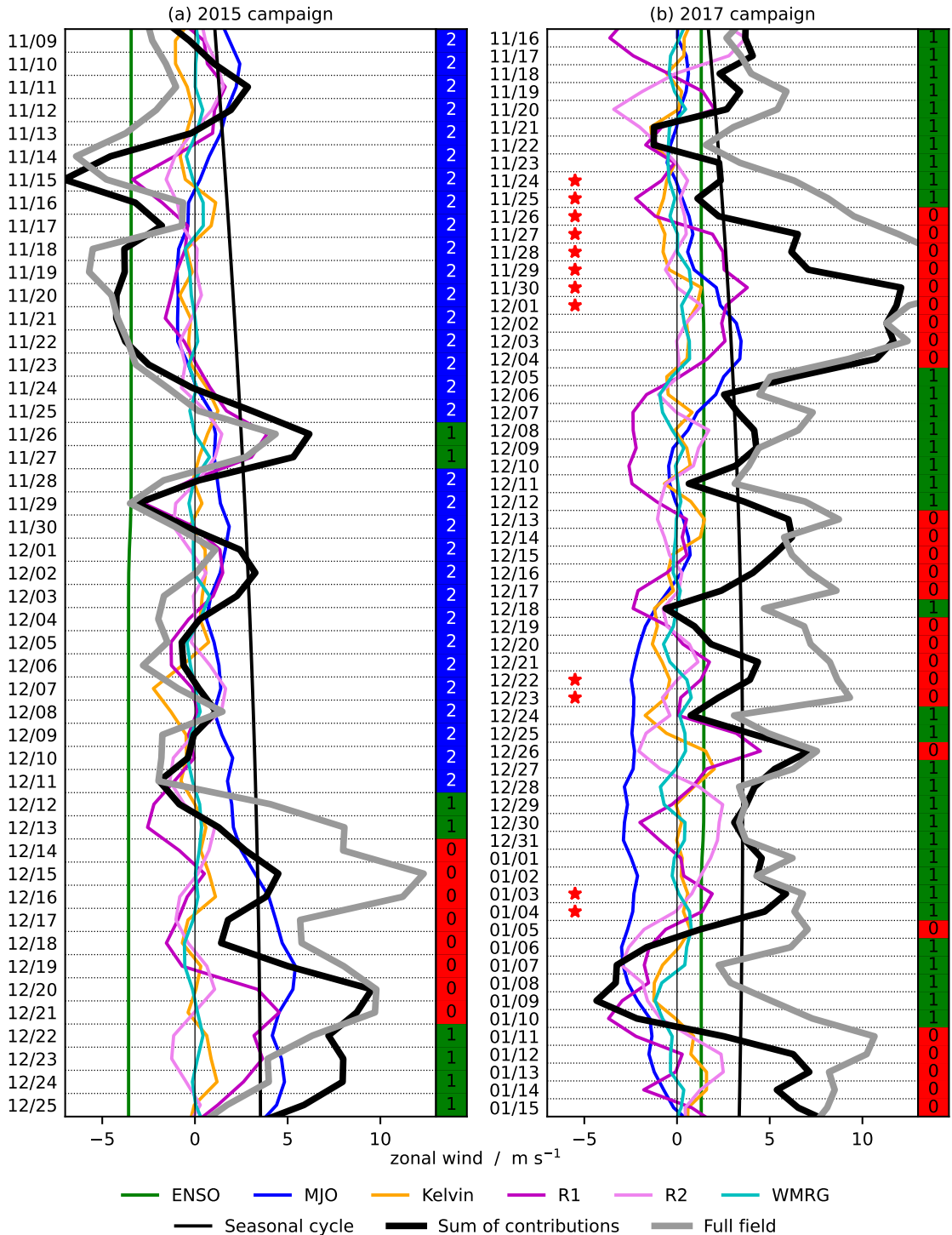




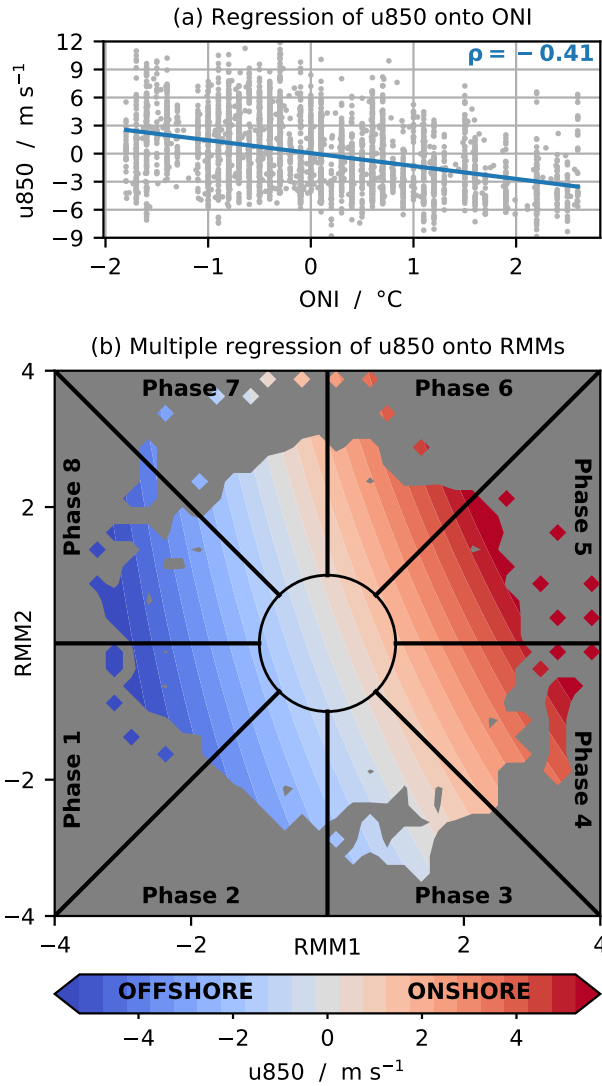
912 FIG. 2. (a–c) Diurnal cycle of vertical profile of zonal wind from radiosondes at Bengkulu during the 108 days  
 913 2015/09/11–2015/12/25 and 2017/11/16–2018/01/15. Days are sorted into 3 clusters using the *k*-means algorithm  
 914 (see main text for details), with the number of days in each cluster shown above each panel. Clusters are ordered  
 915 according to the mean value of zonal wind averaged over time and pressure. Radiosonde data are every 3 hours  
 916 and interpolated to the same pressure levels used by the ERA5 reanalysis, from 1000 to 500 hPa, as indicated by  
 917 the tick marks. Local time is taken to be UTC+7. (d–f) As (a–c) but plotted as a diurnal anomaly; that is, with  
 918 the respective daily mean profile for each cluster subtracted.



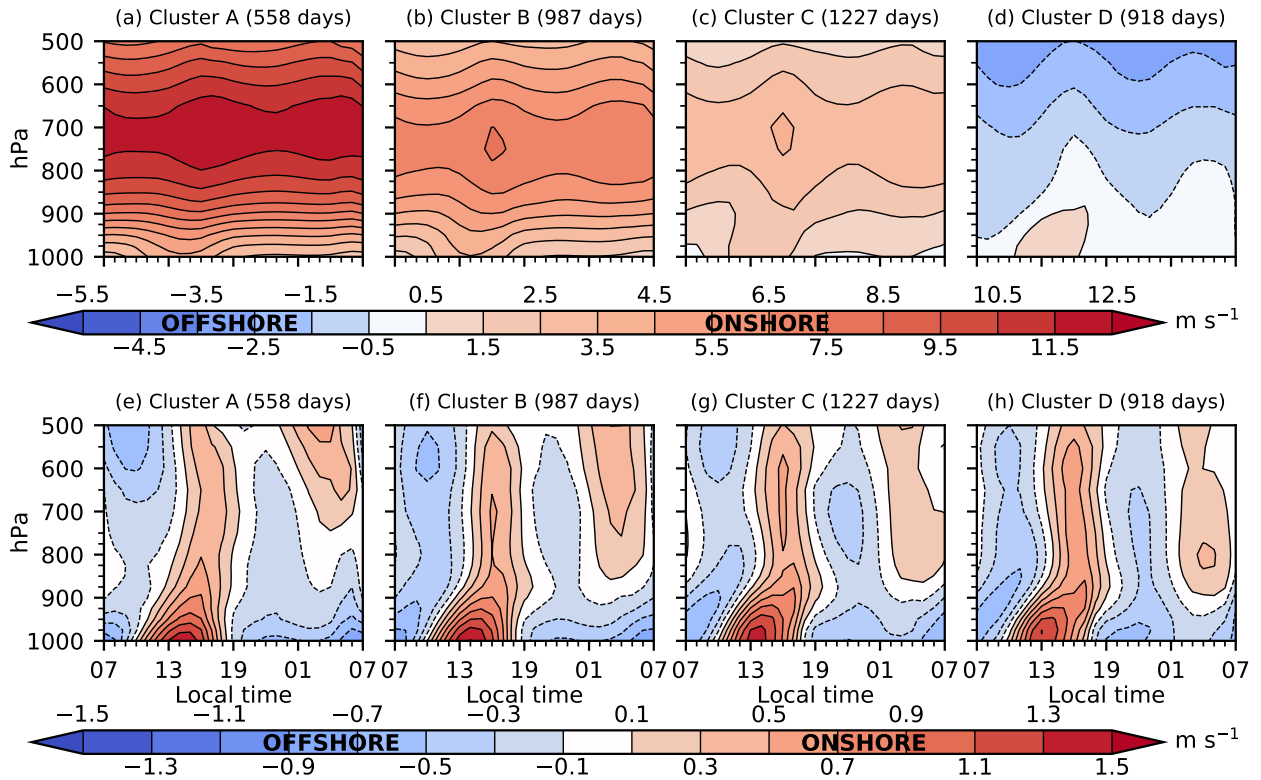
919 FIG. 3. Hovmöller diagrams of the composite diurnal cycle of precipitation from IMERG for each of the  
 920 clusters in figure 2, extended by 12 hours to 19 LT (12 UTC) the following day. Precipitation is composited over  
 921 the red dashed box in figure 1 and averaged along the coastline, every 30 minutes. The mean orography is shown  
 922 below each panel in metres above sea level (ASL).



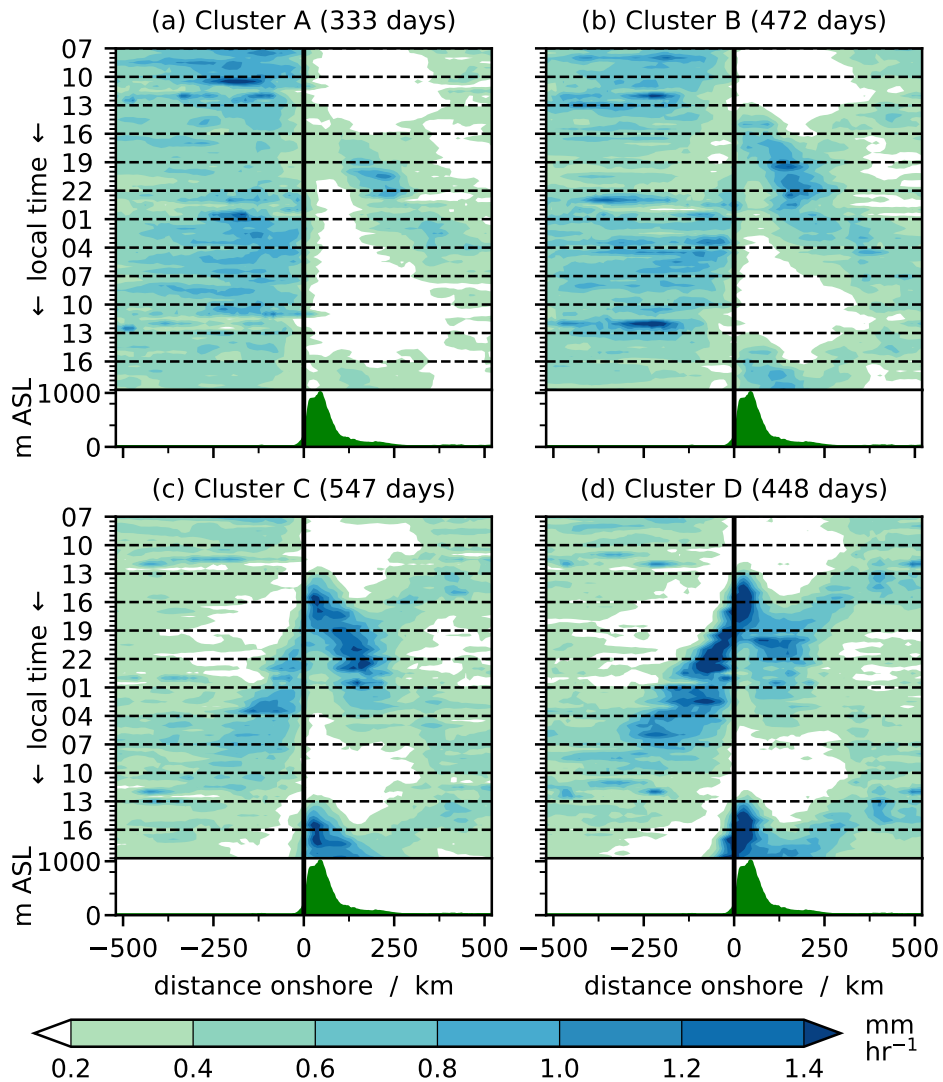
923 FIG. 4. Time series of  $u_{850}$  (grey) from ERA-Interim at Bengkulu during the two field campaigns. Coloured  
 924 curves show  $u'_{850}$  due to ENSO (dark green; regression onto ONI), the MJO (dark blue; multiple regression onto  
 925 RMMs), equatorial Kelvin (orange), R1 (dark pink), R2 (light pink) and WMRG (light blue) waves (identified in  
 926 ERA-Interim). **Thin black dotted**-curve shows the mean seasonal cycle. **Thick black solid**-curve is the sum  
 927 of the six coloured curves and the mean seasonal cycle. Red stars indicate a TC centre within  $10^\circ$  geodesic of  
 928 Bengkulu. (All TCs shown are in the southern hemisphere.) Red, green and blue boxes denote clusters from  
 929 figures 2a–c.



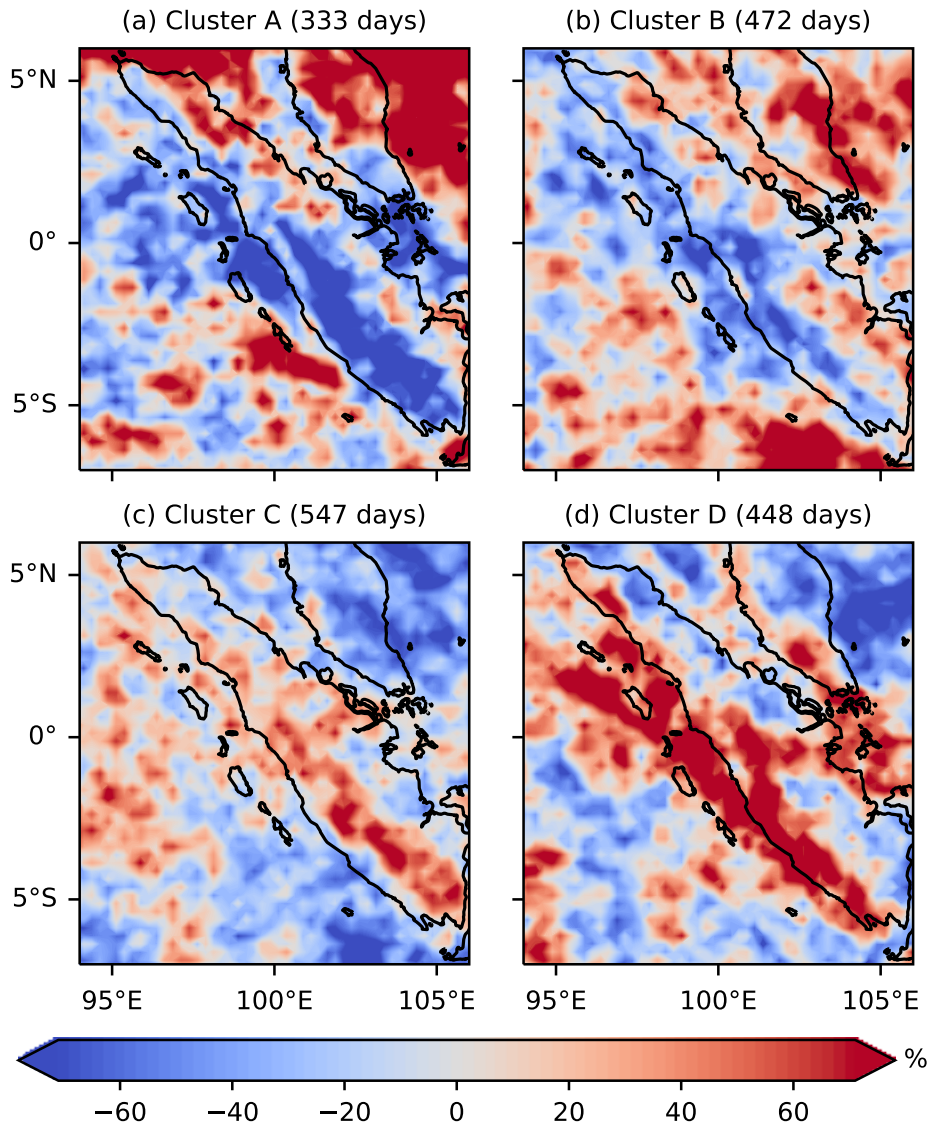
930 FIG. 5. (a) Linear regression of south-west Sumatra coast  $u'_{850}$  onto ONI index of ENSO, according to equation 1.  
 931 The data points used for the regression are shown in grey.  $\rho$  is the correlation coefficient. (b) Multiple linear  
 932 regression of south-west Sumatra coast  $u'_{850}$  onto RMM indices of the MJO, according to equation 2. Areas with  
 933 no MJO days in the 39 DJFs used are greyed out.



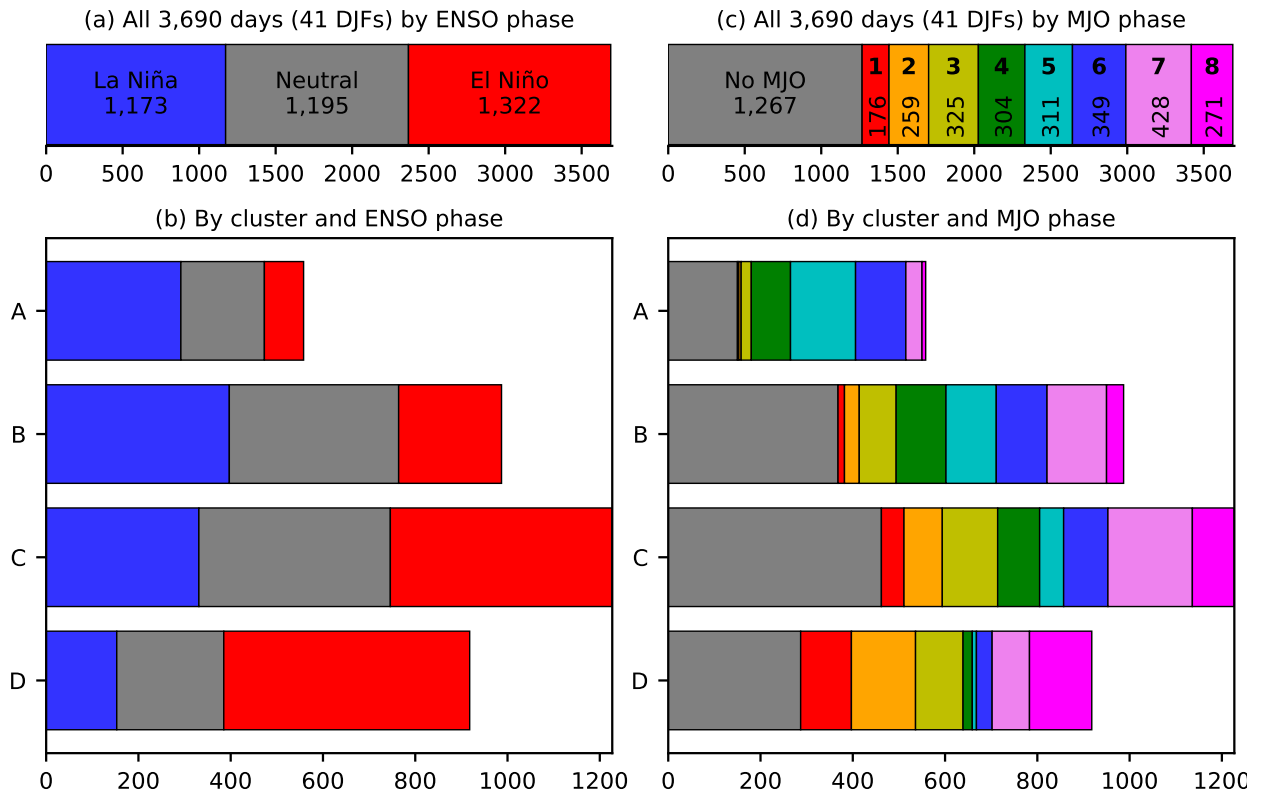
934 FIG. 6. (a–d) Hourly ERA5 zonal wind averaged along the nominal coastline of the solid red box (south-west  
 935 Sumatra) in figure 1, clustered using the  $k$ -means algorithm. 41 DJFs (1979/80–2019/20, excluding 29 February)  
 936 are used with  $k = 4$  (see main text for details of the choice of  $k$ ) and clusters labelled A, B, C and D to avoid  
 937 confusion with the  $k = 3$  clustering in figure 2. (e–h) As (a–d) but plotted as a diurnal anomaly; that is, with the  
 938 respective daily mean profile for each cluster subtracted.



939 FIG. 7. Hovmöller diagrams of the composite diurnal cycle of precipitation from GPM-HQ for each of the  
 940 clusters in figure 6. These composites use a subset (20 DJFs) of the days in figure 6 as GPM is not available  
 941 before the year 2000.

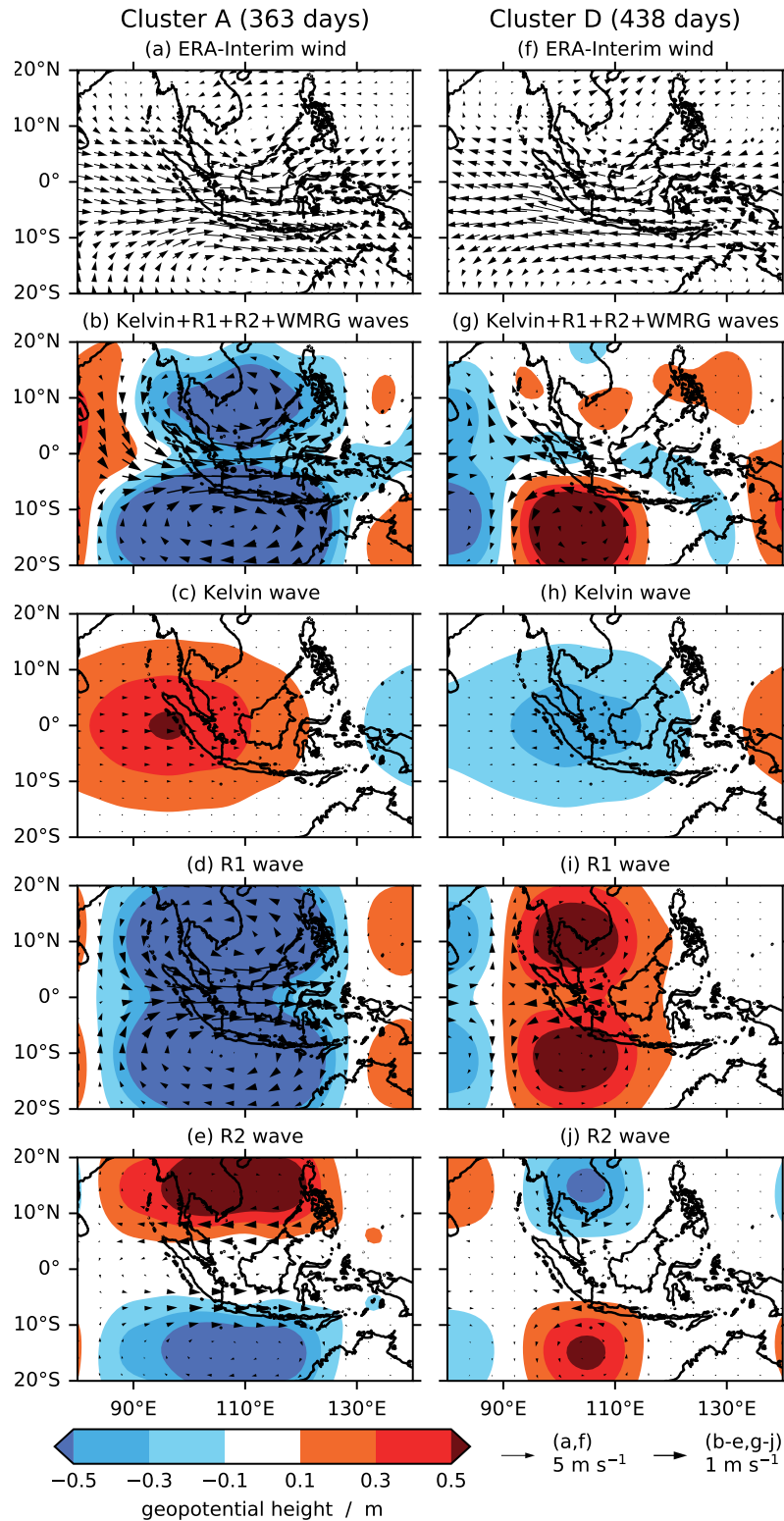


942 FIG. 8. Fractional change (expressed as a percentage), relative to climatology, of the probability of extreme  
 943 precipitation occurring in each cluster, using daily mean **IMERG**GPM-HQ rainfall for the 20 DJFs from 2000/01  
 944 onwards. Extreme precipitation is defined as exceeding the 99<sup>th</sup> percentile, so the climatological probability is  
 945 0.01 everywhere. Data are regridded to 0.25° for plotting purposes.

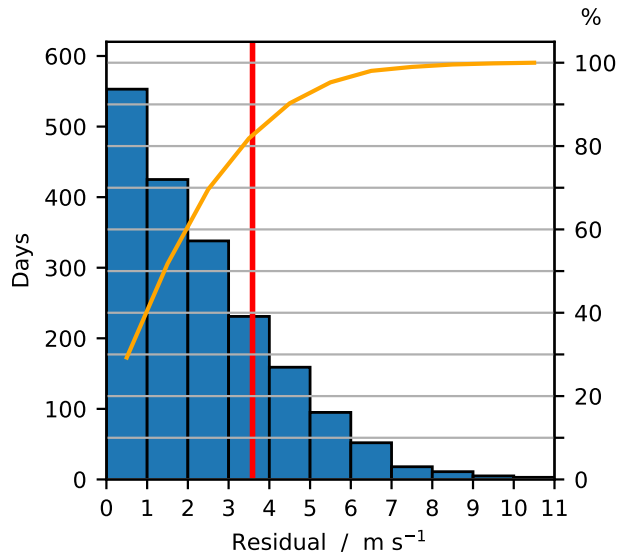


946 FIG. 9. (a) Number of days in DJFs 1979/80–2019/20 in each phase of ENSO. (b) As (a) but separately for  
 947 each of the clusters in figure 6. (c,d) As (a,b) but for the MJO, with grey indicating RMM amplitude < 1. MJO  
 948 large-scale convection is active over the Indian Ocean in phases 2–3, the MC in 4–5, the western Pacific Ocean  
 949 in 6–7, and the western hemisphere and Africa in 8–1; and is suppressed in the corresponding opposite phases.





950 FIG. 10. Composites at 850 hPa for clusters A and D from figures 6a,d. (a,f) Daily mean horizontal wind  
 951 anomaly using ERA-Interim reanalysis data. (b,g) Daily mean horizontal wind and geopotential height anomalies  
 952 from structures of equatorial waves, summed over Kelvin, R1, R2 and WMRG waves. (c,h) As (b,g) but for  
 953 Kelvin wave contribution only. (d,i) As (b,g) but for R1 wave contribution only. (e,j) As (b,g) but for R2 wave  
 954 contribution only. All composites use a subset (21 DJFs) of the days in figure 6, for 1997/98 to 2017/18.



955 FIG. 11. Histogram of the absolute value of the residual south-west Sumatra coast  $u_{850}$ , with the theoretical  
 956 value computed as the sum of the contributions from the MJO, ENSO, equatorial Kelvin, R1, R2 and WMRG  
 957 waves, and the mean seasonal cycle. For the example days shown in figures 4 and S1, this is the absolute  
 958 difference between the grey and ~~solid~~thick black curves. Blue bars show the number of days in each bin (left  
 959 vertical axis); orange curve shows the cumulative distribution as a percentage (right vertical axis); and red line  
 960 shows the inter-annual standard deviation of  $u_{850}$ , averaged over each day of DJF.

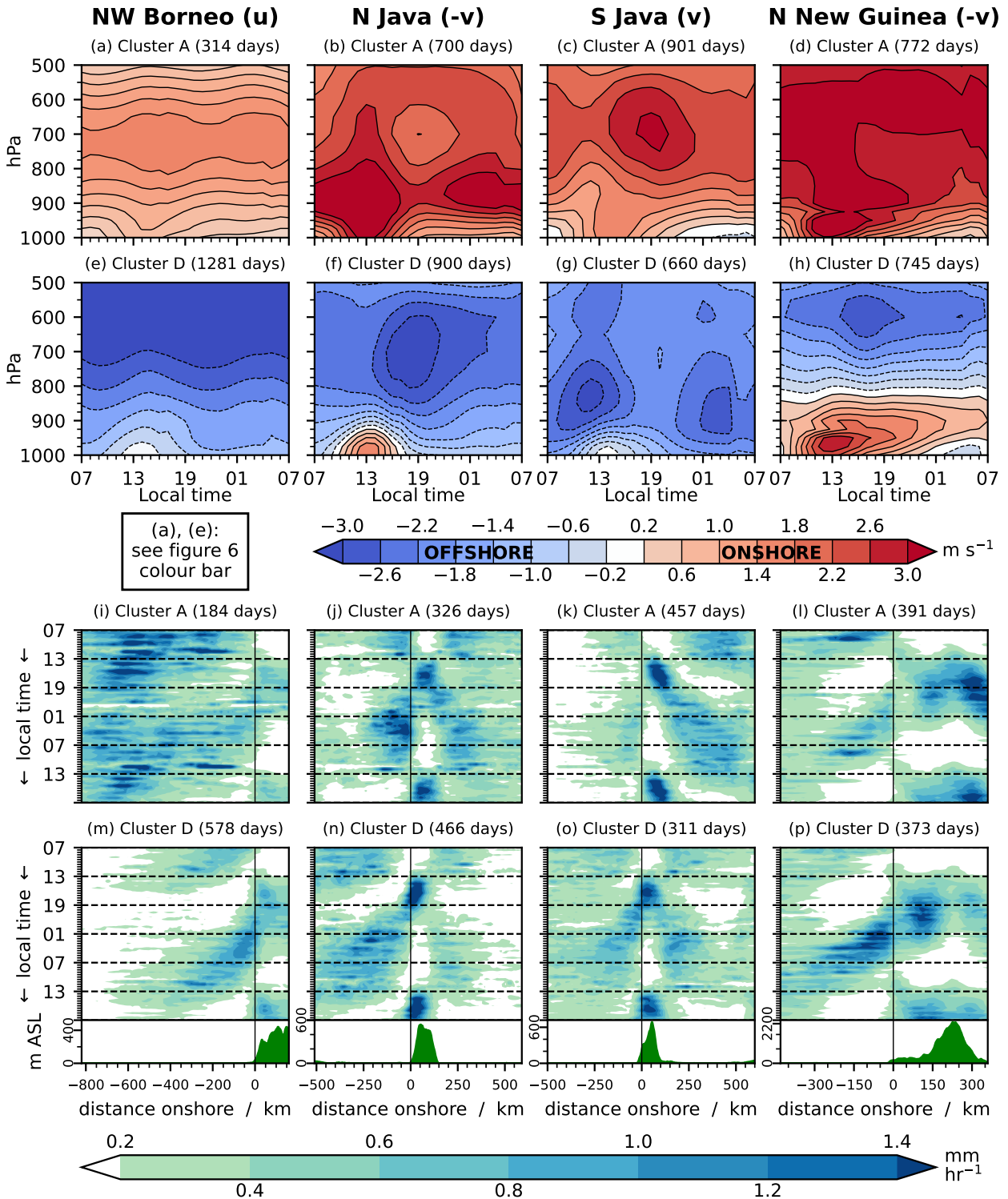
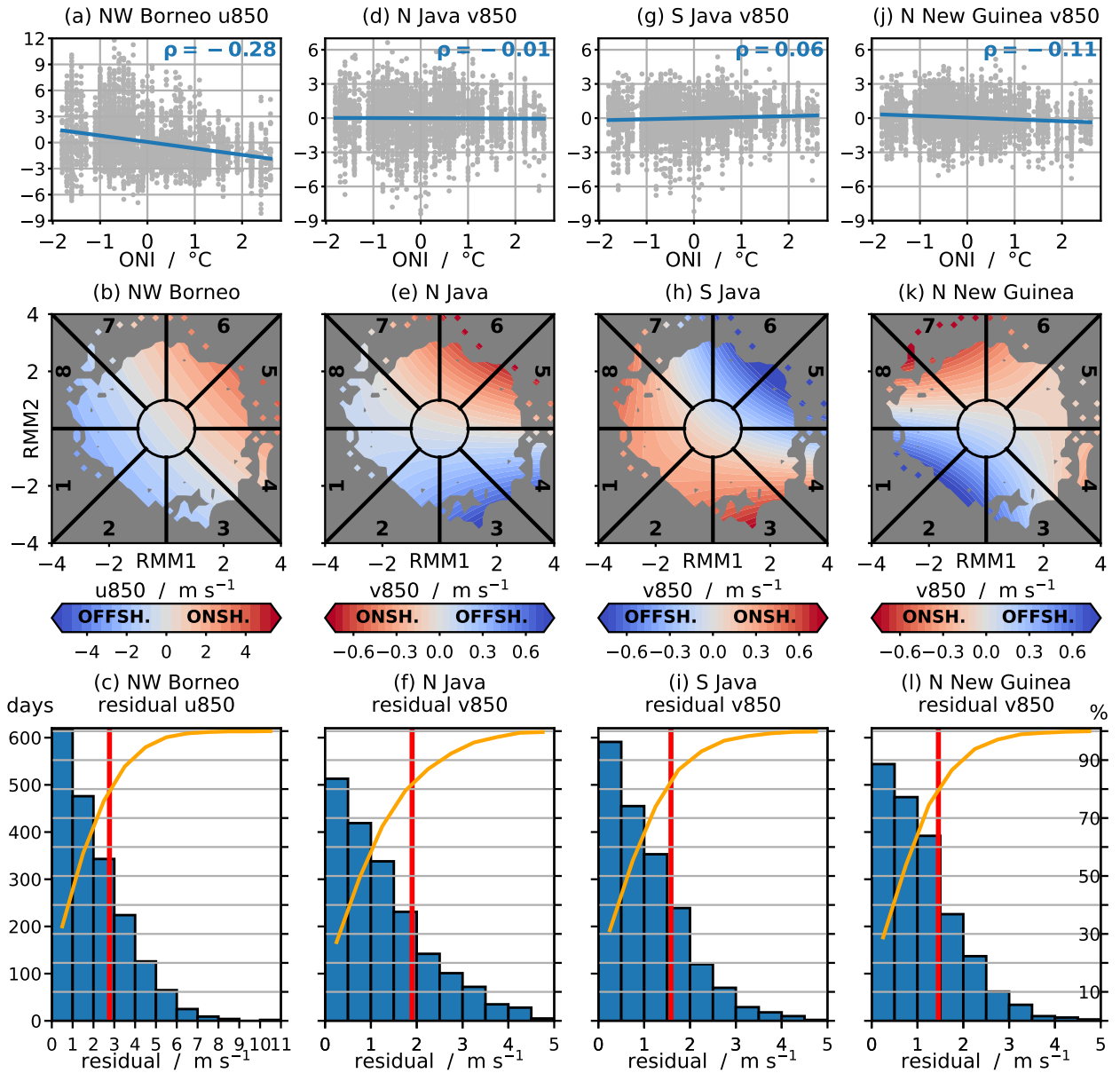
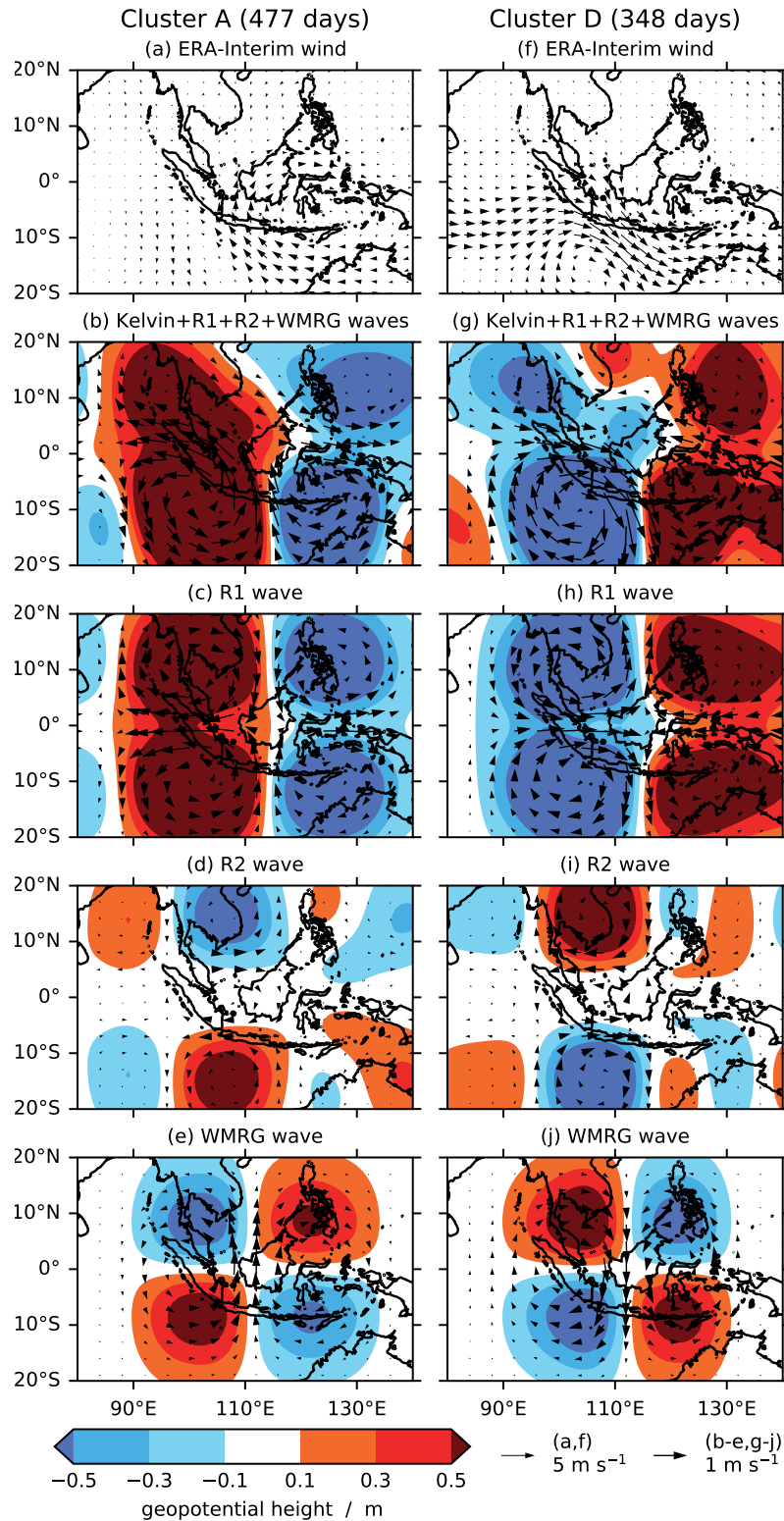


FIG. 12. (a–h) As figure 6 but extended to the other coastlines shown in figure 1, for  $k = 4$  (clusters B and C not shown).  $u$  and  $v$  after each coastline name indicate whether zonal or meridional wind was clustered. Wind in the onshore direction is plotted in red and the offshore direction in blue, with cluster A as the most onshore cluster. For north Java and north New Guinea this requires the sign to be reversed so  $-v$  is plotted. Note that panels (a) and (e) use the same colour bar (not shown here) as figure 6. (i–p) As figure 7 but for the clusters shown here in panels a–h.



967 FIG. 13. Top two rows as figure 5 and bottom row as figure 11, but for (a–c) north-west Borneo, (d–f) north  
 968 Java, (g–i) south Java and (j–l) north New Guinea. For middle row, colours are chosen so that red is always  
 969 onshore wind. For bottom row, tick marks up to 600 (number of days in each bin; left axis) relate to blue bars;  
 970 and horizontal grid lines and tick marks up to 100 (cumulative distribution as a percentage; right axis) relate to  
 971 orange curves.



972 FIG. 14. (a,b,f,g) As figure 10 but for south Java clusters A and D (see figures 12c,g). (c,h) R1, (d,i) R2 and  
 973 (e,j) WMRG contributions only.

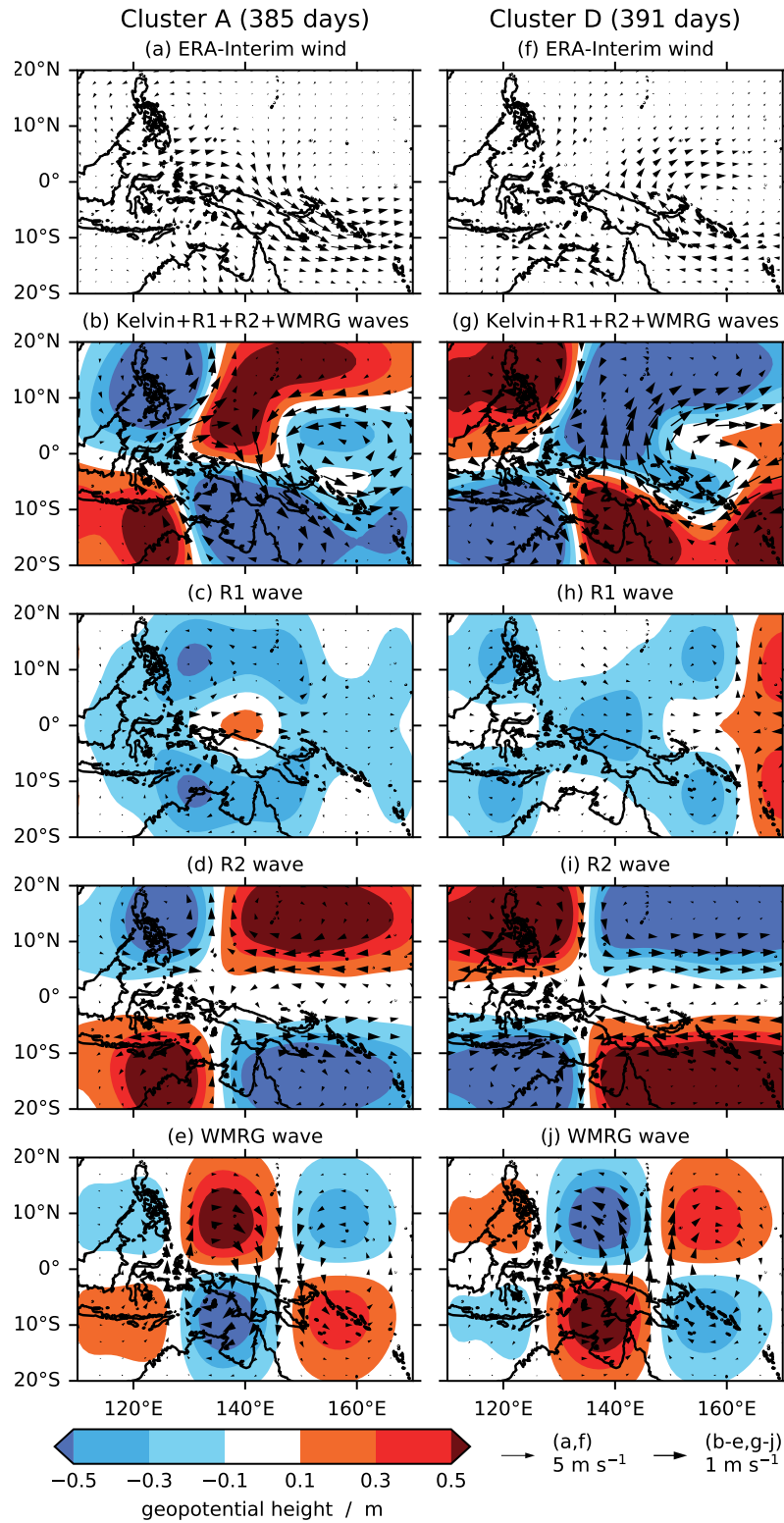
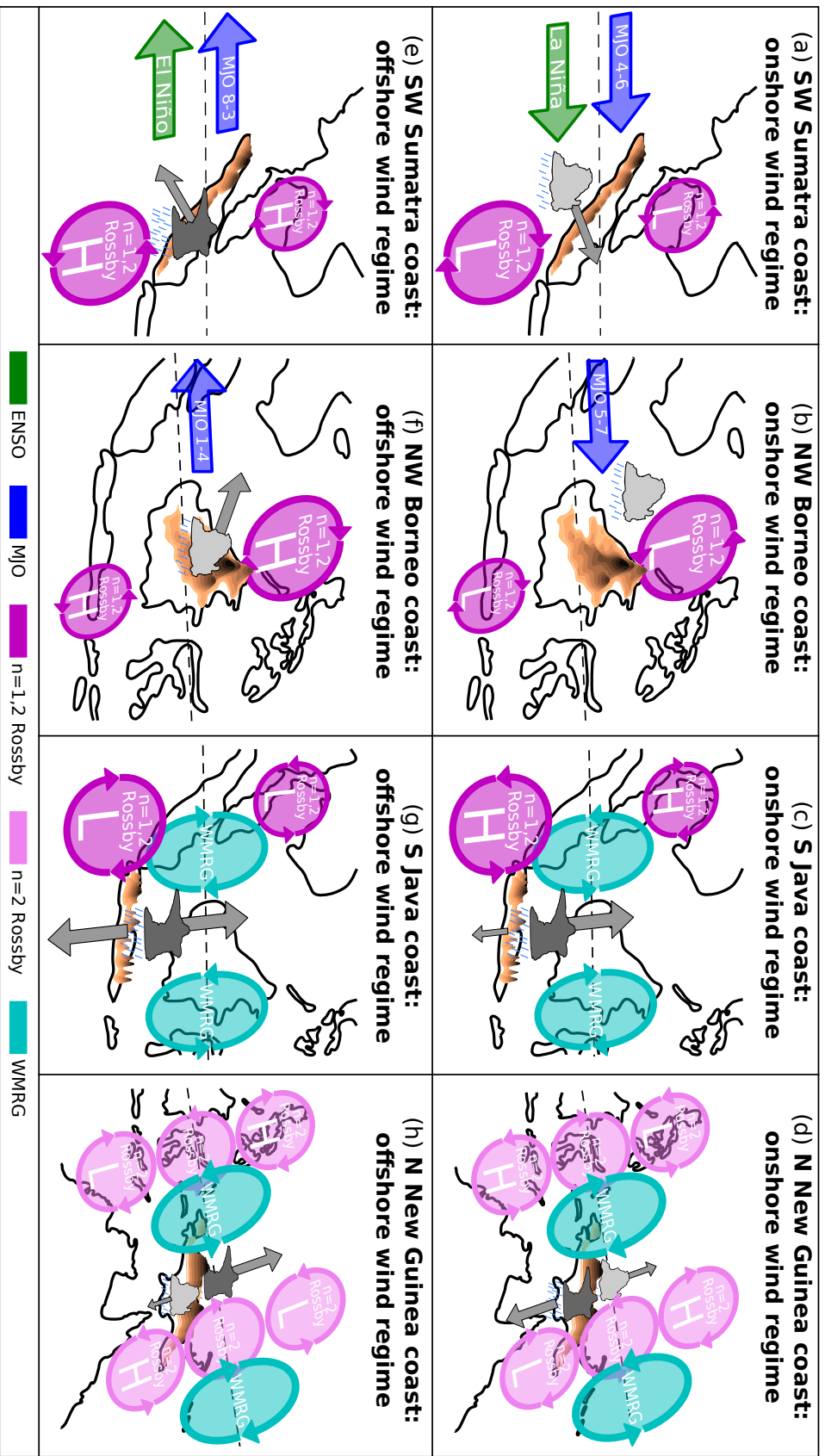


FIG. 15. As figure 14 but for north New Guinea clusters A and D (see figures 12d,h).

Coastline	Driver and % variance	Onshore regime (suppressed DC)	Offshore regime (enhanced DC)
South-west Sumatra	R1+R2* (43.3%)	Cyclonic phase (strong in SH)	Anti-cyclonic phase (strong in SH)
	MJO (24.8%)	Phases 4–6	Phases 8–3
	ENSO (17.2%)	La Niña	El Niño
North-west Borneo	R1+R2* (40.4%)	Cyclonic phase (strong in NH)	Anti-cyclonic phase (strong in NH)
	MJO (10.0%)	Phases 5–7	Phases 1–4
North Java	WMRG (32.4%)	High pressure NW & SE Low pressure SW & NE	High pressure SW & NE Low pressure NW & SE
	R1+R2* (29.2%)	Cyclone centre slightly to W (strong in SH)	Anti-cyclone centre slightly to W (strong in SH)
South Java	R1+R2* (48.3%)	Anti-cyclone centre slightly to W (strong in SH)	Cyclone centre slightly to W (strong in SH)
	WMRG (25.8%)	High pressure SW & NE Low pressure NW & SE	High pressure NW & SE Low pressure SW & NE
North New Guinea	WMRG (44.0%)	High pressure N & SE Low pressure S & NE	High pressure S & NE Low pressure N & SE
	R1** (14.9%)	—	—
	R2 (10.3%)	High pressure SW & <u>N</u> /NE Low pressure NW & <u>S</u> /SE	High pressure NW & <u>S</u> /SE Low pressure SW & <u>N</u> /NE

974 FIG. 16. Summary of the large-scale drivers with the strongest control on coastal wind regime, and the phases  
975 associated with the strongest onshore and offshore regimes, for each of the coastlines analysed. Forcings are  
976 listed if the variance in their associated  $u'_{850}$  or  $v'_{850}$  (depending on the coastline) is at least 10% of the variance  
977 in the full  $u_{850}$  or  $v_{850}$  field during DJFs 1997/98 to 2017/18; for a full list, see table S4. Colours correspond  
978 to the boxes in figure 1, with more intense shades highlighting larger contributions to the variability. \*For  
979 coastlines other than north New Guinea, identified R2 waves appear to be an artefact of the same circulation  
980 pattern which projects more strongly onto the theoretical R1 structure, so the two are shown in combination.

981 \*\*For north New Guinea, although the variance associated with R1 waves is high enough to be listed here, their



964 Fig. 17. Schematic diagram of important large-scale drivers, and their effect on convection and its propagation, for strong onshore and offshore  
 965 coastal wind regimes for the Maritime Continent coastlines detailed in figure 16. North Java is not shown due to its similarity to the results for south  
 966 Java (with onshore and offshore reversed). Dark grey cumulonimbus clouds indicate intense convection and rainfall; light grey cumulus clouds indicate  
 967 more moderate rainfall. Grey arrows indicate propagation, with the largest arrow in an image indicating the strongest propagation (not to scale between  
 968 images). These are drawn with reference to the Hovmöller diagrams in figures 7 and 12i–p. Coloured arrows indicate the wind direction associated with  
 969 large-scale drivers. H and L refer to high and low pressure centres. For  $n = 1, 2$  Rossby waves these differ in size between hemispheres (see main text  
 970 for details). MJO numbers refer to phases from Wheeler and Hendon (2004). The dashed line marks the equator. Major mountains are shown for each  
 971 island (relative size between images not to scale).